LAWRENCE
LIVERMORE
NATIONAL
LABORATORY

LLNL-TR-509016

Research and Development of Non-Spectroscopic MEMS-Based Sensor Arrays for Targeted Gas Detection

A. Loui, S. K. McCall

October 27, 2011

Disclaimer

This work performed under the auspices of the U.S. Department of Energy by Lawrence Livermore National Laboratory under Contract DE-AC52-07NA27344.

32200 (DSW-MTP)
FY11 Report: Noble Gas Detection (540809)

Research and Development of Non-Spectroscopic MEMS-Based Sensor Arrays for Targeted Gas Detection

A. Loui and S.K. McCall

1.1 Introduction

The ability to monitor the integrity of gas volumes is of interest to the stockpile surveillance community. Specifically, the leak detection of noble gases, at relevant concentration ranges and distinguished from other chemical species that may be simultaneously present, is particularly challenging. Aside from the laboratory-based method of gas chromatography-mass spectrometry (GC-MS), where samples may be collected by solid-phase microextraction (SPME) or cryofocusing, the other major approaches for gas-phase detection employ lasers typically operating in the mid-infrared wavelength region. While mass spectrometry can readily detect noble gases – the helium leak detector is an obvious example – laser-based methods such as infrared (IR) or Raman spectroscopy are completely insensitive to them as their monatomic nature precludes a non-zero dipole moment or changes in polarizability upon excitation.

Therefore, noble gases can only be detected by one of two methods: 1) atomic emission spectroscopies which require the generation of plasmas through laser-induced breakdown, electrical arcing, or similar means; 2) non-spectroscopic methods which measure one or more physical properties (e.g., mass, thermal conductivity, density).

In this report, we present our progress during Fiscal Year 2011 (FY11) in the research and development of a non-spectroscopic method for noble gas detection. During Fiscal Year 2010 (FY10), we demonstrated via proof-of-concept experiments that the combination of thermal conductivity detection (TCD) and coating-free damped resonance detection (CFDRD) using micro-electromechanical systems (MEMS) could provide selective sensing of these inert species. Since the MEMS-based TCD technology was directly adapted from a brassboard prototype commissioned by a previous chemical sensing project, FY11 efforts focused on advancing the state of the newer CFDRD method. This work, guided by observations previously reported in the open literature, has not only resulted in a substantially measureable increase in selectivity but has also revealed a potential method for mitigating or eliminating thermal drift that does not require a secondary reference sensor. The design of an apparatus to test this drift compensation scheme will be described. We will conclude this report with a discussion of planned efforts in Fiscal Year 2012 (FY12).

1.2 Project Scope

Determining the hermeticity of known gas volumes requires the measurement of an observable that essentially satisfies the following requirements: 1) the containment vessel is leak-tight (i.e., hermetic) if the observable does not change in value; 2) the containment vessel is leaking if the observable changes in value, with a leak rate related to the observable rate of change. This definition precludes processes such as outgassing and sorption which generate or

consume gases (i.e., sources and sinks, respectively). An observable that ostensibly satisfies these requirements is pressure; a single pressure sensor (e.g., a capacitive manometer) exposed to the internal gas environment of the containment vessel can detect changes in pressure than can be correlated to the presence of a leak. Conversely, a single pressure sensor external to the containment vessel may also detect changes that could be definitively correlated to leaks thereof, but only in the absence of other potentially leaking gas volumes. However, the successful use of pressure to monitor hermeticity requires that any breaches in the gas integrity of a containment vessel will give rise to *pressure*-driven leaks; put another way, a difference in absolute pressure across a containment vessel wall must exist if measured pressure changes are to be correlated to the presence of a leak through the wall. Pressure-based leak monitoring fails in the case where a loss of hermeticity occurs between contiguous volumes of gases at the *same pressure*, since *diffusion*-driven leaking will occur under isobaric conditions. Moreover, the presence of gas sources and sinks will lead to pressure changes independent of any loss in leak-tightness, introducing further ambiguity into a pressure-based monitoring approach.

These difficulties can be remedied by selecting an observable which can assume values that at least partially correlate to the chemical identity of a gas. In the common example of mass spectrometry, the essential measurement of atomic or molecular mass in the form of a spectral cracking pattern of ionized fragments is strongly correlated to the identity of the chemical species; this chemical selectivity, enhanced by hyphenation with gas chromatography, has established GC-MS as the preeminent laboratory-based method of chemical analysis. Unlike the pressure-based approach, a selective leak detection method can detect both pressure- and diffusion-driven leaks by monitoring changes in chemical composition. The gas composition within a system of contiguous containment vessels, as a design specification, is known at the time of first production or refurbishment; therefore, any subsequent change wherein a gas type known to be in one vessel is detected in an adjacent vessel, signals the likelihood of a breach in mutual leak-tightness. The correlation of changes in chemical composition to a leak is further strengthened if pairs of sensors are used, each simultaneously exhibiting complementary changes within their respective containment vessels; nevertheless, a single strategically-placed sensor can operate successfully if the various gases are sufficiently distinctive such that any advective or diffusive exchange with the environment outside the system, or with internal sources and sinks, can be readily discerned. The identification of "unexpected" gas-phase chemical species – that is, those not obviously present by design or a facile derivative process such as hydrolysis – also provides an additional benefit to material aging and compatibility research efforts. While GC-MS is the currently deployed method for gas analysis in the U.S. complex,[1] this unwieldy benchtop-scale technology is inappropriate for leak monitoring across multiple dispersed units and with a potentially high duty cycle of operation. The current work on MEMS-based sensors addresses the unfulfilled need for an eminently deployable leak detection technology.

1.2.1 Temporal Evolution of Pressure-Driven Gas Leaks

Before appropriate sensors can be selected for a gas leak detection application, the characteristics of the leak must be defined. Perhaps the most important property of a leak is its rate, since this will determine the necessary frequency of operation; additionally, the ability to discern a leak will depend on the temporal relation of the leak rate to any drift in the sensor response. If a leak is very slow, a leak might be mistaken for such drift; in such a case, a low duty cycle is warranted (e.g., weekly) so that more substantial and hence less ambiguous changes can be observed. Alternatively, a very rapid leak requires a high-frequency or continuous mode

of sensor operation if the loss of hermeticity is to be *actively* detected. However, the swift attainment of a steady state ensures that a comparatively lower duty cycle will find the monitored containment vessel in some distinct but stable condition: either the specified gas composition (pre-leak), or an aberrant gas composition (post-leak).

Several factors determine the leak rate through a breach in the wall of a gas containment vessel, chiefly: 1) the size of the breach; 2) a pressure gradient across the breach (pressure-driven leak) and/or; 3) a chemical potential gradient across the breach (diffusion-driven leak). In this work, we will restrict our attention to purely pressure-driven leaks; the obvious aftermath of any such leak will be a comparatively slower diffusive mixing under isobaric conditions. That the leak rate is directly related to the breach size is intuitively obvious, while the pressure and/or chemical gradients for any potential intervessel leak are known from design specifications; less evident are the circumstances and forces which can create a breach. Stress corrosion cracking of austenitic stainless steels and nickel-chromium alloys, particularly at locations of high residual stress (e.g., welds), is a well-known phenomenon in the nuclear and aerospace industries;[2-4] however, the corrosive environment of a maritime atmosphere or within a water-cooled nuclear reactor is absent in the present application. Thus, in addition to defects that may be introduced at the time of manufacture, assembly, or refurbishment, mechanical insults are the primary expected cause of leaks. It is difficult to predict the location and occurrence of a breach beyond general analyses of structural loads, fatigue, and stress risers; further, the size of a breach, whether microscopic or readily visible to the naked eye, cannot easily be deduced from the loading which created it.

Nevertheless, it is instructive to examine the temporal evolution of a pressure-driven leak as a function of breach size. For illustrative purposes, consider the two contiguous containment vessels at 20°C shown in Figure 1. Vessel 1 has a volume V_1 = 1 ft^3, while vessel 2 has 10 times the volume (V_2 = 10 ft^3) and a gas pressure of P_2 = 15 psia (~1 atm). Suppose that vessel 1 has 10 times the pressure of vessel 2 (P_1 = 150 psia), and a breach suddenly opens in the adjoining wall. Assuming that the gas in vessel 2 is N_2, Figs. 2 and 3 show the changes in P_1 and P_2 as a function of time for various common gases in vessel 1 leaking through an idealized circular hole 7 μm and 70 μm in diameter, respectively; these correspond to 100:1 and 10:1 aspect ratio holes through a 0.028" wall thickness, which is a common value for small-diameter stainless steel tubing. The non-linear leak behavior is calculated using the iterative numerical method described in Appendix A. While the time to achieve a steady-state ($P_1 = P_2$) is expectedly slow for a micro-

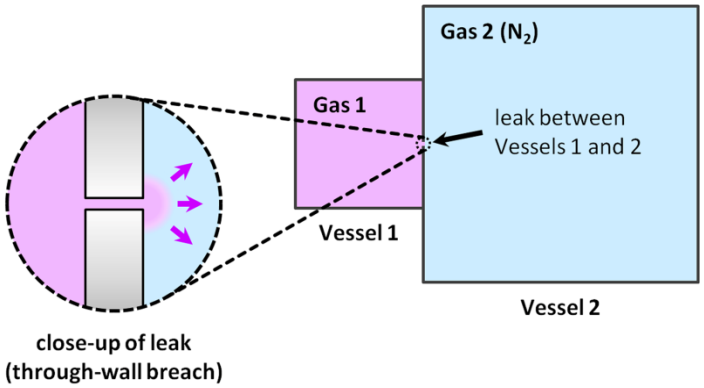

Figure 1. Hypothetical leak between contiguous gas containment vessels.

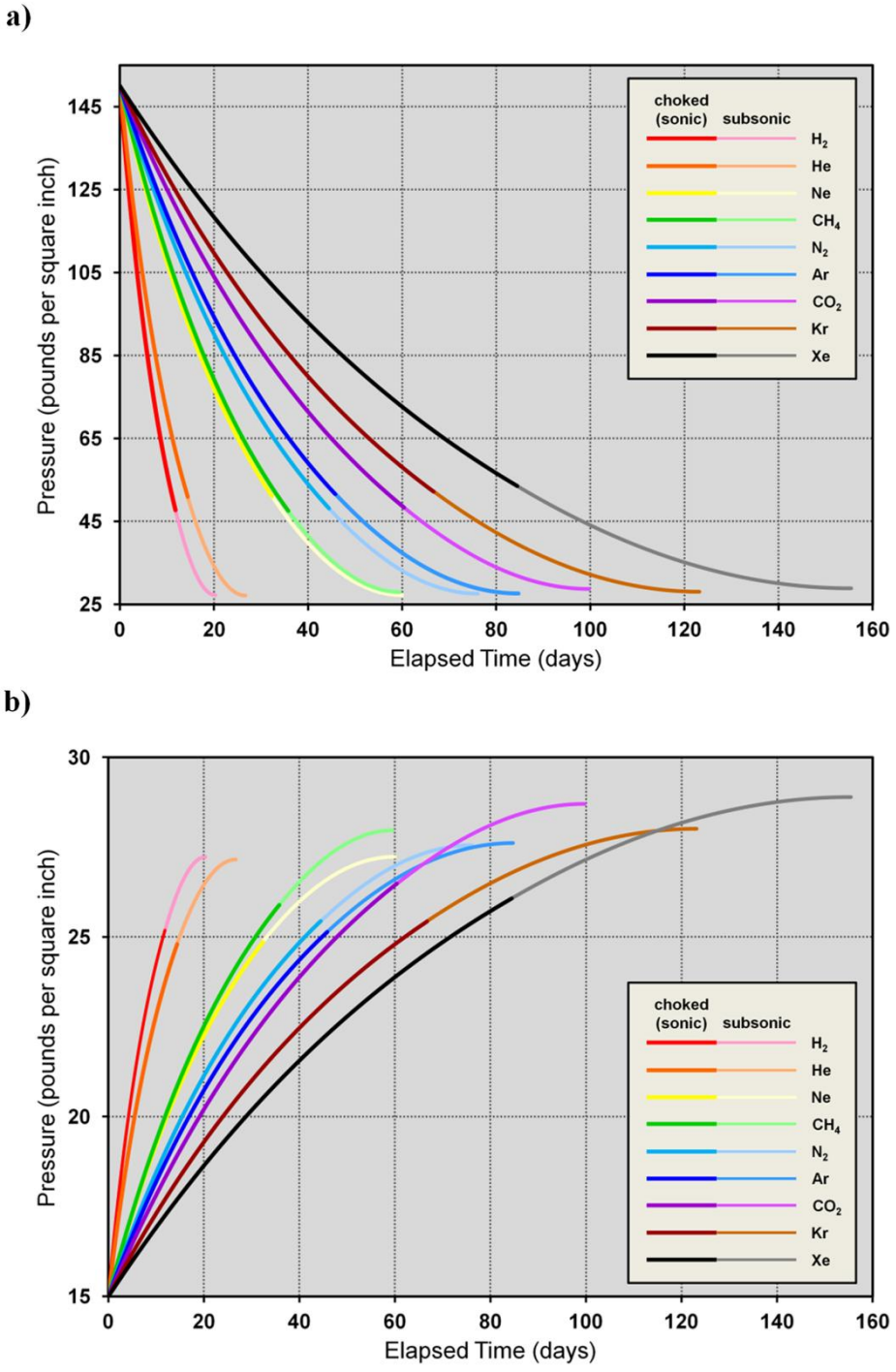

Figure 2. Temporal evolution of a pressure-driven leak at 20°C for various gases initially at 150 psia into a vessel initially containing 15 psia N_2, corresponding to a 7 μm intervessel circular breach. a) Pressure of vessel 1 (P_1). b) Pressure of vessel 2 (P_2).

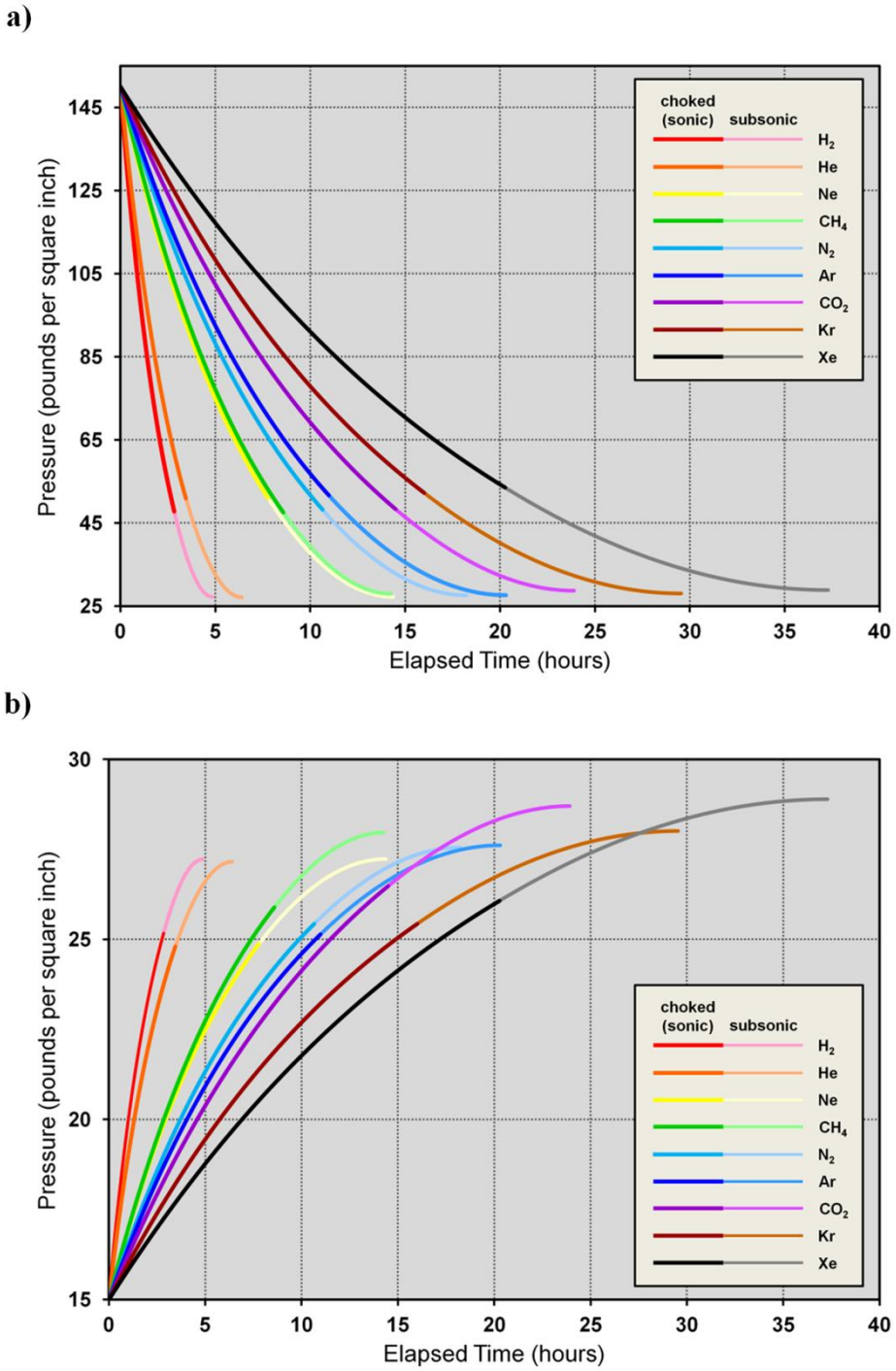

Figure 3. Temporal evolution of a pressure-driven leak at 20°C for various gases initially at 150 psia into a vessel initially containing 15 psia N_2, corresponding to a 70 μm intervessel circular breach. a) Pressure of vessel 1 (P_1). b) Pressure of vessel 2 (P_2).

scopic pinhole (up to ~5 months), a hole large enough to be seen unaided leads to a leak that may be completely resolved in a matter of hours. In the latter case, which one might expect to occur as the result of a severe mechanical insult leading to rupture, a leak sensor operating discontinuously would most likely register an abrupt stepwise change in response corresponding to the stable pre- and post-leak gas compositions (sources and sinks notwithstanding). If this example is generalized to systems containing multiple contiguous vessels, each filled with a different pressurized gas, a single chemically-selective leak sensor could record significant changes of condition and deduce which vessel(s) are leaking into the volume occupied by the sensor based on how the gas composition has changed; a simple pressure transducer, in the same scenario, would register the occurrence of a leak but would be incapable of discerning the source(s).

In the examples above, the change in gas composition of vessel 2 as a function of time for the 7 μm and 70 μm diameter breaches can also be plotted (Figs. 4 and 5, respectively). The concentration of the leaking gas rises rapidly in the gas-N_2 binary mixture, reaching one part-per-thousand (0.1%) within a couple of hours for the microscopic pinhole, and within a minute for the larger breach. The time evolution of the gas composition in a pressure-driven leak therefore defines the requisite sensitivity of the selective leak sensor with respect to its duty cycle. For the foregoing cases, concentrations in the low parts-per-million only exist in the first fractions of a second (70 μm) to a minute (7 μm) immediately following leak induction. Therefore, unless the sensor operates continuously and it is critical that a leak be identified within seconds or minutes of creation, more modest detection limits and reduced operational frequency should be acceptable in any practical concept of operations (CONOPS).

1.2.2 Quantifying Damping Due to Sorbed Contamination

In the current selective leak sensor design, a piezoelectrically-driven silicon microcantilever is used to implement the coating-free damped resonance detection (CFDRD) method. This approach, described in a previous paper,[5] relies on the inertial and viscous damping of the oscillating structure in a gas; the subtle changes in density and viscosity that occur when the gas composition is altered can be readily measured via changes in the resonance condition. The CFDRD method is distinct from the more common resonance detection method based on the sorption of target species to the oscillator via a chemically-functional coating. This method of resonance damping via mass uptake has been widely demonstrated, with various high-affinity coatings used for example to detect airborne vapors of explosives,[6] solvents,[7] and chemical weapons simulants.[8] Beginning with our efforts in FY10, we have presumed that there was negligible sorption of such chemical vapors in the absence of a coating. The possible presence of aerosolized nanoparticles, their potentially turbulent dispersion during mechanical insult and subsequent deposition on the oscillator has not been ruled out, but is not considered further in the current report.

Gases such as N_2 and H_2 are known to have a negligible propensity to condense and adhere, either molecularly or dissociatively, to metal and semiconductor surfaces at room temperature;[9-11] this poor affinity for adsorption is represented by small values of sticking coefficient which saturate at sub-monolayer coverages. From a thermodynamic perspective, this is not surprising given that such gases have low boiling points even at significantly elevated pressures. However, the case of sublimated chemical vapors is less clear since, by definition, these exist at temperatures at or below the point of vaporization. This raises the question as to

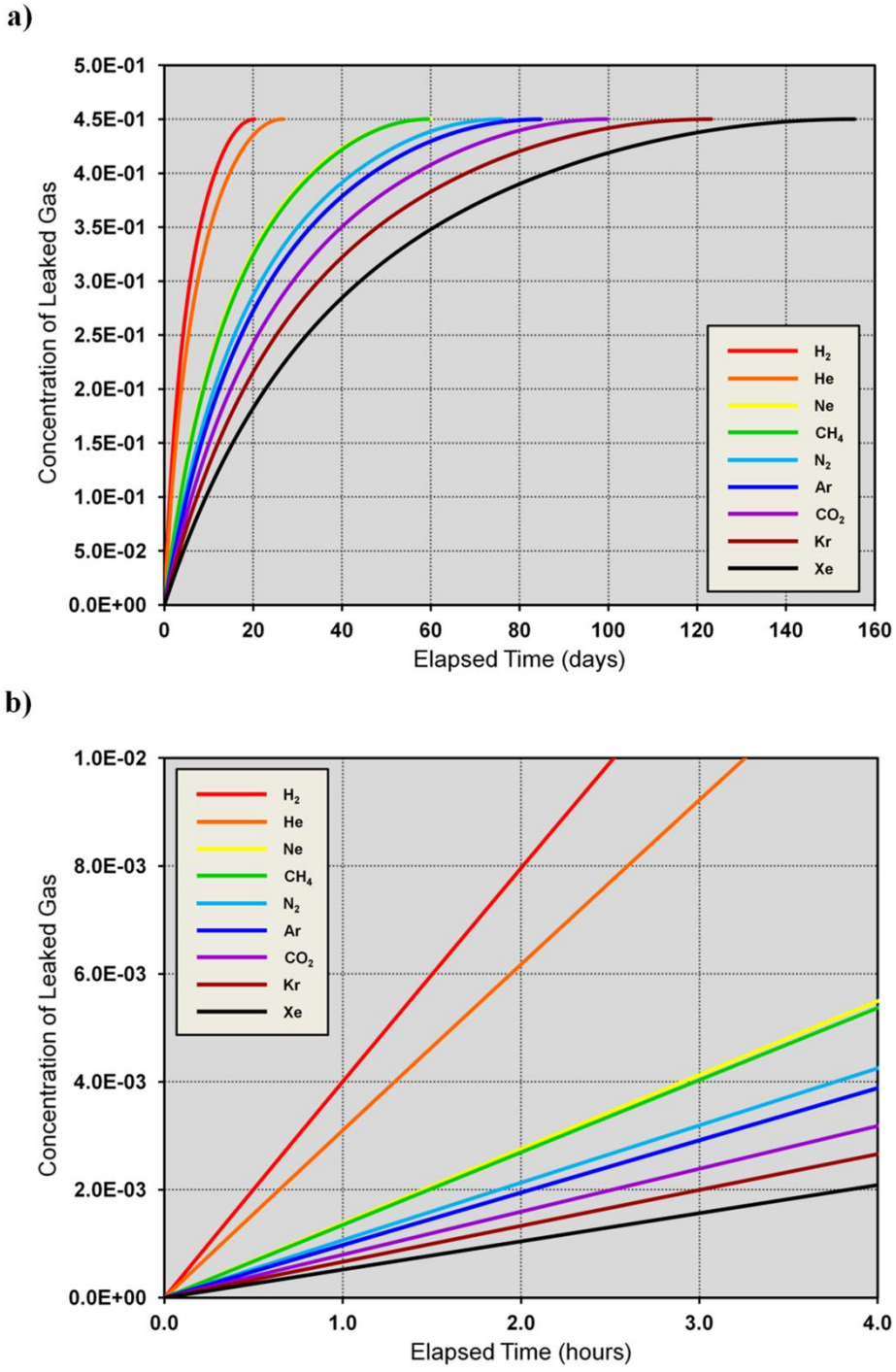

Figure 4. a) Change in gas composition versus time corresponding to a pressure-driven leak at 20°C for various gases initially at 150 psia into a vessel initially containing 15 psia N_2, corresponding to a 7 μm intervessel circular breach. b) Close-up of concentration change immediately following leak induction.

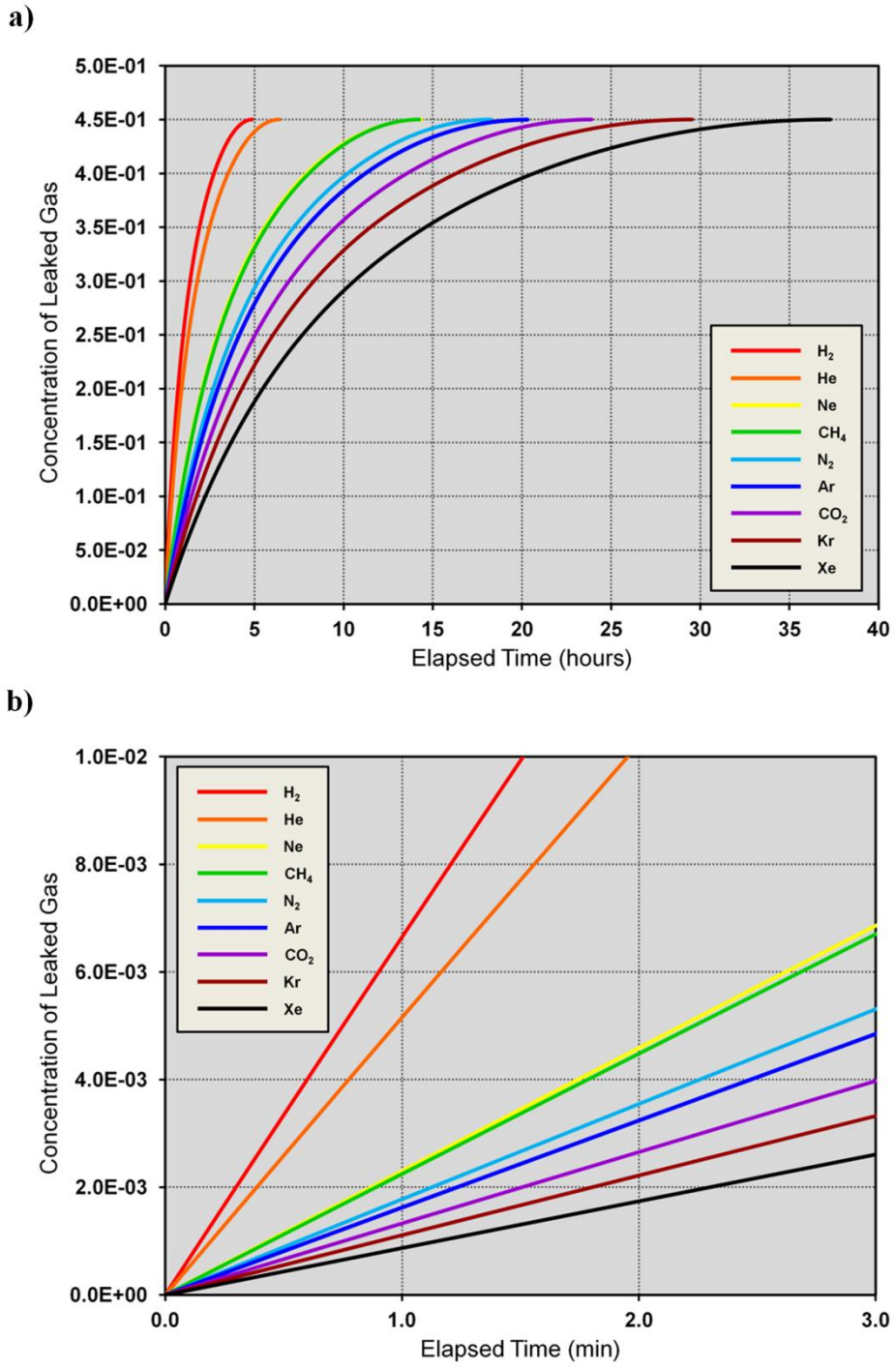

Figure 5. a) Change in gas composition versus time corresponding to a pressure-driven leak at 20°C for various gases initially at 150 psia into a vessel initially containing 15 psia N_2, corresponding to a 70 μm intervessel circular breach. b) Close-up of concentration change immediately following leak induction.

whether such outgassing species could adsorb to the surfaces of the coating-free oscillator at ambient operational temperatures in sufficient quantity to cause a measureable change in the resonance condition; in such an event, inertial/viscous damping could be indistinguishable from damping caused by mass uptake, particularly at lower gas concentrations.

To provide some justification for our exclusion of vapor sorption effects, we can estimate the shift in fundamental resonance frequency of a silicon microcantilever upon adsorption of water. Water vapor is a well-known residual gas in a weapon's headspace,[12] and the adsorption of water on silicon surfaces has been previously studied under the controlled conditions of ultrahigh vacuum (see Ref. 13 and citations therein). For a resonating cantilever with dimensions equivalent to the Veeco/Bruker Active Probe currently used in this project (Section 1.3.1), the fundamental frequency shift is predicted to be approximately -0.2 to -0.4 Hz with submonolayer saturation adsorption of water under ambient atmospheric conditions (Appendix B). In the current breadboard-level sensor prototype, this frequency shift is correlated to a mixture of ~0.3 to 0.7% Ar in N_2 (i.e., 3-7 parts-per-thousand). However, as is also shown in Appendix B, the ideally clean surface of the oscillator, upon exposure to water vapor at typical atmospheric concentrations, becomes saturated in less than a microsecond; thus, unless exceptional protocols entailing vacuum degassing and handling are followed, the DRD transducer should have resonant frequencies that are shifted with respect to the idealized condition from the outset of its operational lifetime. As long as the adsorbate-saturated condition remains stable in situ, the frequency shift will amount to a permanent offset that is transparent to the user. In any case, given the discussion of Section 1.2.1 on likely leak detection CONOPS, the magnitude of any fluctuations in the adsorbate "load" due to interactions with sources and/or sinks is unlikely to have any measureable impact on the ability to detect a leak. Finally, the condensation of any chemical vapor due to cooling will not occur unless the partial pressure of the species exceeds the saturation pressure at the reduced temperature (e.g., the dew point for water vapor). The trace occurrence of vapors in the monitored environment virtually eliminates this possibility except under extreme cooling conditions; such a possibility can be estimated by comparing the measured vapor concentrations against saturation values computed by the empirical Antoine equation (for example).[14]

1.3 FY11 R&D Activities for CFDRD

As stated in Section 1.1, research and development efforts in FY11 focused on advancing the state of the coating-free damped resonance detection method. However, it is important to keep in mind the underlying concept of increasing chemical selectivity – that is, the ability to distinguish one chemical species from another – through the combination of multiple, so-called orthogonal sensing modalities. The exploitation of this concept is the guiding principle for much of the work described in this report.

In a paper published in the second quarter of FY10, we laid out the theoretical underpinnings of the selective gas sensing project.[5] During FY10, these ideas were tested via proof-of-concept experiments which demonstrated that the combination of thermal conductivity detection (TCD) and coating-free damped resonance detection (CFDRD) could provide selective sensing of noble and other gas species. For convenience, these methods are briefly summarized below.

Thermal conductivity detection is a well-established technique where the relative efficiency of heat dissipation by a gas-immersed heating element is correlated to the thermal

conductivity of the environment, providing information about the identity of the gas.[15-17] Coating-free damped resonance detection of gases has also been widely demonstrated using cantilevers,[18-20] quartz crystal tuning forks,[21-23] and silicon columns,[24] where the relative degree of inertial and viscous damping of a gas-immersed oscillating element is correlated to the density and viscosity of the environment, also providing information about the gas identity.

In the following sub-sections, we describe our FY11 efforts in further developing and refining the CFDRD mode:

a) Optimization of analog circuit design and data acquisition (Section 1.3.1);
b) Down selection of potential CFDRD data channels based on maximizing selectivity (Section 1.3.2);
c) Development of strategies to mitigate or eliminate thermal drift in sensor response (Section 1.3.3).

1.3.1 Circuit Design and Data Acquisition

From the inception of the experimental phase of this project, we have used a commercially available atomic force microscope (AFM) microcantilever to serve as the gas-immersed resonating sensor element. Since one of our objectives is to minimize the bulk and complexity of the sensor head, we eschewed optical AFM cantilevers – which are the most prevalent type available – in favor of specialized designs which employ direct piezoelectric actuation and sensing. To the best of our knowledge, there are two such designs currently on the market: the Bruker Active Probe (formerly Veeco) and the NANOSENSORS A-Probe.[25, 26] Both of these designs are based on collocated piezoelectric elements that directly drive the cantilevers into flexural or weak-axis oscillation. We have selected the former cantilever, which has been available for about a decade and has been thoroughly characterized in some recent experimental and theoretical studies.[27-29]

To drive the cantilever at one of its resonance modes and simultaneously detect changes in resonance, we incorporated the device into an alternating-current (AC) bridge circuit with a lock-in amplifier measuring the bridge voltage. At zero frequency, the piezoelectric cantilever behaves like an insulator; at non-zero frequencies, it behaves like a series RLC circuit in parallel with a capacitor.[30] Based on these properties, a circuit similar to a Schering bridge (Fig. 6) was assembled but with $R_3 = 0$ and C_3 replaced by the Active Probe piezoelectric cantilever. Balancing the AC bridge, we found through iterative refinement that the following circuit component values produced a very favorable response: $R_1 = 100\ k\Omega$, $C_1 = 100\ pF$, $C_2 = 4700\ pF$, $R_2 = 100k\Omega$.

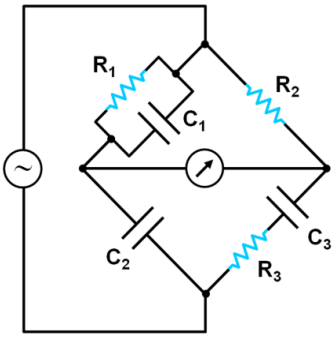

Figure 6. Schering bridge circuit.

Initial measurements were done using a lock-in amplifier (Stanford Research Systems SR830) running at a 1V drive signal amplitude with a reference-relative phase $\phi = 96.53°$ based on a measurement at 10 kHz. The typical response was in the range of 50-60 mV at low frequencies, and decreasing with increasing frequency. The circuit response was examined over a wide frequency span (10 kHz – 100 kHz), and the fundamental resonance in ultrahigh purity N_2 was observed in the range f_{0,N_2} = 55–65 kHz depending on the particular Active Probe cantilever employed. These measured frequency values are consistent with the nominal value specified by the manufacturer,[25] as well as with previous measurements which were directly obtained by laser vibrometry.[27, 28] The in-phase and out-of-phase outputs of the lock-in amplifier correspond to the time-independent real and imaginary components of the bridge voltage, respectively. When the in-phase signal is plotted as a function of drive voltage frequency, we observed substantial shifts in frequency shifts that were consistently observed upon changes in the gas composition (Fig. 7).

As is evident in Fig. 7, the resonance peak is asymmetrical which may make it more difficult to evaluate changes in the resonance condition. A simple LabView code was constructed, allowing fine-tuning of the phase angle to produce a more symmetric peak with a well-defined baseline; the optimal phase adjustment was found at $\phi \cong 9°$ (Fig. 8, top). Even in this state, at frequencies far from the resonance peak, the baseline is not quite flat and the shape of the peak retains a degree of asymmetry. We also note that, not surprisingly, the asymmetry of the out-of-phase output is simultaneously maximized in the same state (Fig. 8, bottom); thus, either output signal could be used to monitor the cantilever resonance with the optimum value of phase angle. The sloping asymmetry and characteristic trough/peak shape in the bridge voltage reflect the electromechanical behavior of the piezoelectric cantilever. Piezoelectrics are well-known to have, for each resonance frequency, an antiresonance frequency occurring at a nearby higher frequency value; these correspond to a local minimum (trough) and maximum (peak) in

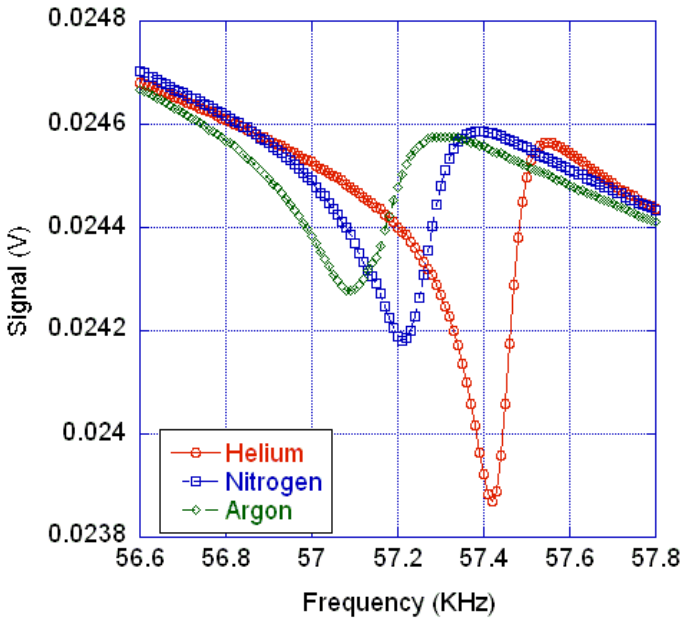

Figure 7. In-phase output of lock-in amplifier, showing the fundamental resonance peak in various ultrahigh purity test gases: Ar, N_2, and He.

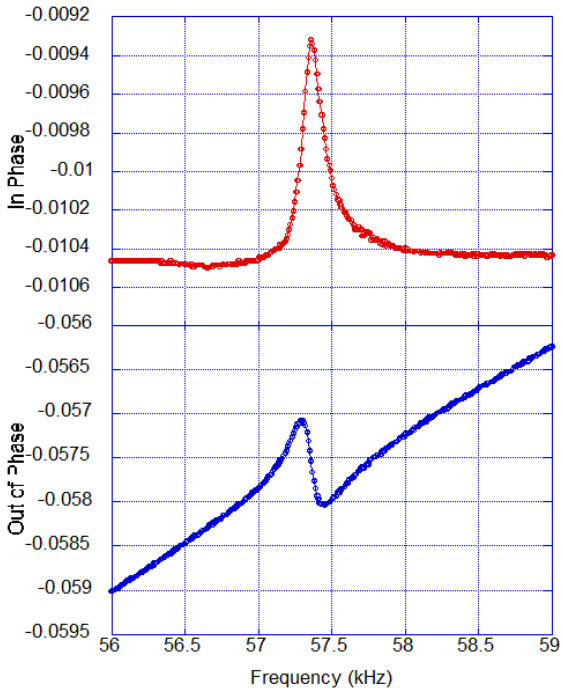

Figure 8. Lock-in amplifier output in ultrahigh purity N_2 after optimization of phase angle with respect to the in-phase signal: in-phase (top); out-of-phase (bottom).

the impedance spectrum, respectively.[30] Therefore, the voltage across the piezoelectric cantilever will also display a trough followed by a peak as the drive voltage frequency is increased through a resonance/antiresonance pair. The phase adjustment described above thus amplifies the relative prominence of the resonance peak while simultaneously minimizing the antiresonance peak.

The SR830 lock-in amplifier has a frequency limit of approximately 100 kHz; since the next normal mode frequency above the fundamental for the Active Probe cantilevers occurs at ~210 kHz,[25, 28, 29] access to higher resonances requires alternative instrumentation. To investigate these resonant modes, the lock-in amplifier was replaced with a function generator (Agilent 33120A: 100 μHz – 15 MHz sine wave output) and oscilloscope (Tektronix TDS 3012B). Initial calibration measurements at f_{0,N_2} yielded very small signals that were not usable. The original test set-up using the lock-in amplifier was re-tested at $\phi \cong 9°$, and the well-defined fundamental resonance peak was reproduced; this indicated that there was a problem with the new instrumentation and not with the circuit (e.g., recently damaged cantilever). The original test set-up was incrementally transformed into the new set-up in order to isolate and diagnose the problem: 1) the bridge voltage output was simultaneously connected to the lock-in amplifier and oscilloscope, resulting in a noisy and unusable signal; 2) the oscilloscope was disconnected, and the resonance peak re-appeared. These troubleshooting steps suggested the presence of a ground loop(s) between the instruments. Through further methodical investigations in which the circuit and its connections to the function generator and oscilloscope were completely disassembled and rebuilt, the ground loop(s) were eliminated. As was discovered, the simple reversal of common and signal leads for each instrument resulted in a complete obfuscation of the bridge voltage signal.

In the recent study by Sanz and co-workers, the first seven resonance modes of the Active Probe cantilever were calculated by finite element analysis (FEA) and experimentally measured by both direct (laser vibrometry) and indirect (impedance analysis) means.[29] The latter approach ascertains the mechanical resonances of the cantilever through electrical measurements of its piezoelectric oscillator element; although these authors used an expensive commercial tool (Agilent 4294A impedance analyzer: ~$45K USD), the basic philosophy of an indirect electrical measurement mirrors our own approach. Their findings are summarized in Table 1 below for convenient reference:

Table 1. First seven normal modes of the Bruker Active Probe, as analyzed by Sanz et al. (Ref. 29)

Mode Number ⇒	**1**	**2**	**3**	**4**	**5**	**6**	**7**
FEA	55.9	209.2	237.8	437.3	666.4	958.9	1102.5
laser vibrometry (kHz)	55.4	205.8	237.9	405.2	639.8	915.2	1097.3
impedance analysis (kHz)	55.4	–	237.9	405.2	–	915.2	1097.3

A similar, earlier study by Jalili and co-workers examined frequencies only up to 500 kHz;[27, 28] their finite element analysis and laser vibrometry measurements revealed first and second normal modes that closely match the results of Sanz et al. However, the third normal mode was reported to have a frequency of 382.5 kHz, which approximately matches the *fourth* normal mode found by Sanz et al. (405.2 kHz). The more recent work by Sanz and co-workers does not cite the work by Jalili et al., so it is uncertain why the third resonance at 237.9 kHz claimed by the former authors was not detected by the latter even though instruments from the same vendor with similar displacement resolution were used (PolyTec MSV-400 and MSA-400, respectively).

Guided by the prior investigations of Sanz et al., we used the new experimental set-up to explore the higher resonance modes of the Active Probe cantilever. The primary motivation for this task was to determine whether or not the various resonances exhibited the same degree of inertial/viscous damping, within a single scaling factor, upon immersion in the gases of interest; any pair of normal modes that deviate from this linearly dependent behavior are orthogonal and may be exploited to increase the selectivity of the TCD/CFDRD gas leak sensor. This issue will be discussed more fully in Section 1.3.2.

A secondary motivation for examining resonances beyond the fundamental mode is based on a recent report by Naeli and Brand in which a method was presented for mitigating or eliminating thermal drift in resonant sensors.[31] This method of compensation, which was demonstrated using cantilevers coated for mass uptake, is based on thermally-induced frequency drift that is substantially identical across the various resonance modes of a single oscillator. Such a method of thermal drift compensation is ideal, since it does not require a secondary reference sensor. Our goal was to determine whether the same behavior could be extended to coating-free cantilievers. These findings are described in Section 1.3.3.

Coarse scans in ultrahigh purity N_2 were made for frequencies below the fundamental mode up through the low MHz range, followed by higher-resolution sweeps near each of the expected normal mode frequencies listed in Table 1. These scans revealed only three discernable resonances, with the following peak frequencies: 64.150 kHz, 398.900 kHz, 1190.600 kHz. Based on these values, it appeared that we had discovered the fundamental, fourth, and seventh normal modes (respectively) previously reported by Sanz and co-workers. The absence of an observed mode near 240 kHz contradicts these authors' findings but, as discussed above, is

consistent with the parallel studies by Jalili and co-workers.[27, 28] At present, we cannot explain our inability to detect the 6th resonance; according to Sanz et al., this normal mode has an average flexural displacement that is slightly less than that of the 4th mode, but a relatively larger impedance phase change.[29] Based on this behavior, one would expect these two modes to have comparable magnitudes yet in our data the absence of a peak in the 900–1000 kHz range is as self-evident as the sharp resonance near 400 kHz.

This leaves the 2nd and 5th resonances, which Sanz and co-workers claim cannot be measured by an impedance-based measurement.[29] Their FEA reveals that these modes that are characterized by distal torsional displacements, which they argue lead to anti-symmetric distributions of induced surface charge at the piezoelectric electrodes and hence a nullification of impedance response. We find the basic premise a bit suspect; it is difficult to understand how a cantilever with perfect symmetry about its longitudinal central axis, when driven by a centrally-positioned piezoelectric film into flexural oscillation, could develop any twisting component of motion. While their FEA models were characterized by such perfect bilateral symmetry, Sanz and co-workers acknowledge that asymmetries exist in real cantilevers due to manufacturing imperfections. Structural asymmetry leading to a non-zero torsional component of oscillatory motion is a certainty, but why such twisting should lead to a complete cancellation of electrical response for some modes but not others is unclear. One possibility involves the dual-width design of the Active Probe cantilever: a 375 μm long by 250 μm wide basal segment bearing the piezoelectric film, with a more slender distal segment measuring 125 μm by 55 μm wide.[27] The displacement profile along the length of the cantilever is attenuated for the basal segment compared to the narrower free segment, since the increased width leads to greater flexural and torsional rigidity; an additional consequence is that the nodes and antinodes are not evenly spaced. We speculate that the distal torsional oscillation due to imperfect bilateral symmetry is suppressed for most modes except ones that place the terminal node at a "sweet spot" near the end of the wide segment where the stiffness is reduced (cf. FEA results in Fig. 2 of Ref. 29).

Moving forward from these unresolved discrepancies, we use the identifications made by Sanz et al. and repeated measurements of the 1st, 4th, and 7th resonances in ultrahigh purity Ar and He. These results, along with the resonance data for N_2, are shown in Fig. 9. In the study by Naeli and Brand, the temperature coefficient of frequency was found to be substantially equivalent for all cantilever resonances; in contrast, the effect of analyte mass uptake by a sorptive coating was different for each mode.[31] This difference allows the detection response to be retained while eliminating the thermal drift upon subtraction of any one resonance signal from another. These authors specified that this effect holds only if the sorptive coating is partial: if the uptake of analyte mass is uniformly distributed over the length of the oscillating cantilever, the mass-induced decrement in frequency will be similarly uniform across all resonances, thereby defeating the compensation strategy. In the coating-free case, there is no partial coating to spatially confine the influence of the analyte to only a portion of the cantilever; nevertheless, our original hope was that the inertial and viscous damping by the gas analyte might still somehow create non-identical responses between the various normal modes. The proof-of-concept experiments in FY10 revealed a -110Hz shift for Ar and +200 Hz shift for He relative to N_2 in the 1st mode, which were confirmed in these experiments. The 7th mode peak amplitudes were considerably smaller than the 1st mode (~30%), so it was difficult to discern definitive changes in resonance resulting from changes in the gas identity. What is surprising is that the 4th mode, which provides a much stronger signal than the 1st mode (by almost a factor of 6), displays no

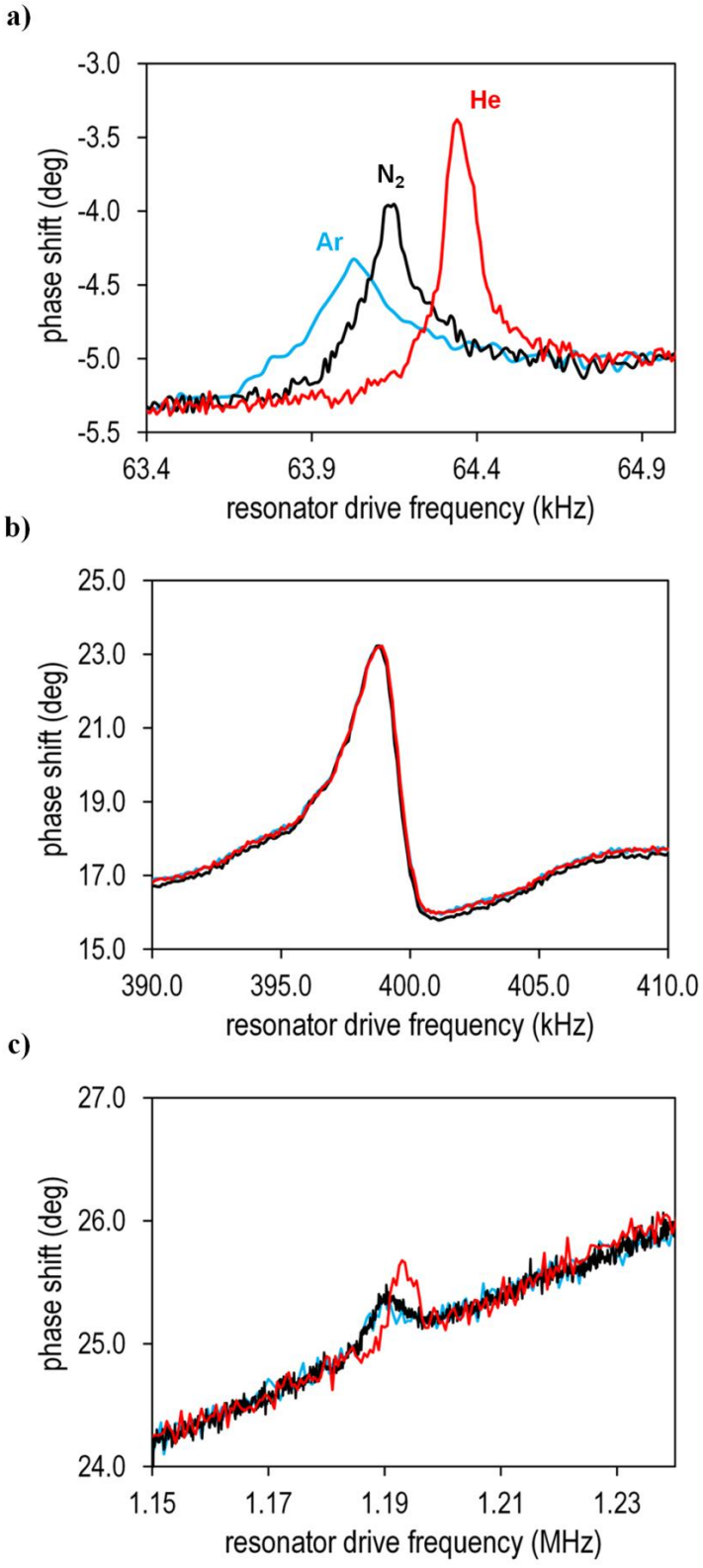

Figure 9. Resonance spectra for three normal modes of the Bruker Active Probe cantilever, immersed in ultrahigh purity Ar, N_2, and He. Note that the lock-in amplifier output is expressed alternatively in terms of phase shift (cf. Figs. 7 and 8). a) 1st normal mode. b) 4th normal mode. c) 7th normal mode.

measureable change as the gas composition is altered. This null result in the coating-free case indicates that an entirely different mechanism than that observed by Naeli and Brand is at play; obviously, non-zero mass uptake for a coated cantilever will always result in a non-zero frequency shift, regardless of whether such shifts for different resonances are identical or not. For thin cantilevers undergoing weak-axis oscillation, inertial damping is expected to dominate over viscous drag effects;[18] therefore, resonance modes which are characterized by large amplitude displacements (and, hence, greater displacements of adjacent gas volume) should be more sensitive to changes in damping conditions than ones with smaller displacements. Sanz and co-workers report laser vibrometry measurements of average flexural displacement, with values of approximately 10.5 and 0.6 nm for the 1st and 4th modes (respectively), which lends credence to this theory.

Regardless of the underlying physical reason, it is clear that our efforts at examining the various resonances – driven by the primary motive of discovering orthogonal normal modes – failed to yield any viable candidates beyond the fundamental mode; obviously, selectivity cannot be increased through the addition of a data channel (the 4th mode) that is intrinsically insensitive to changes in gas composition. However, the secondary motivation – to develop thermal drift compensation – may still be satisfied if the 4th mode proves to have the same temperature coefficient of frequency as the 1st mode. If so, the simple subtraction of signals for these two modes should provide the desired compensation effect. This is actually the most common form of differential compensation, where the reference signal possesses the same drift as the sensor signal but has zero sensitivity to the analyte. In comparison, the mass-uptake case of Naeli and Brand is characterized by candidate pairs of resonances which have the same drift but where both the reference and sensor have sensitivity – albeit non-identical – to the analyte.[31] What is most remarkable about both the coating-free and mass-uptake cases is that the reference and sensor signals are generated by a single resonator, rather than by physically distinct transducer elements as in a typical differential compensation scenario; thus, thermal drift can be mitigated or eliminated without the need for a secondary reference sensor. In Section 1.3.3, we will discuss our initial efforts towards testing the relative, thermally-induced frequency drift of the 1st and 4th resonances.

Finally, as shown in Fig 8 above, adjustments in the phase can yield a lock-in amplifier output with a symmetric peak shape. In all experiments to date, changes in cantilever resonance behavior have been ascertained by generating frequency spectra before and after changes in the test gas composition. In an actual leak detection event, complete resonance spectra would have to be created by scanning the drive frequency and simultaneously reading out any damping response with whatever rapidity is demanded by the duty cycle. Combined with high frequency resolution, this method of data acquisition will generate large amounts of data and potentially slow the sensor down with unnecessarily long dwell times. To address this issue, we have begun investigating the use of simple functions that could be fit with high fidelity to lower resolution resonance peaks in the frequency spectrum. As a first step, we have designed a LabView tool that allows the user to edit a pre-existing resonance spectrum and immediately discern the qualitative effects on the overall selectivity of the TCD/CFDRD gas leak sensor. The determination of the optimum number and frequency distribution of sparse data for the 1st and 4th resonances in all gases of interest is currently slated for completion in early FY12. Although the prescription for lower resolution spectra has yet to be determined, we have already made some unsuccessful attempts at curve fitting including the Gaussian and Lorentzian functions, and

variations thereof. The rapid, cyclic monitoring of a sparse number of fixed frequencies, in conjunction with the functional fits, should greatly improve the data acquisition efficiency.

1.3.2 Optimization of CFDRD Selectivity

In the previous section, we showed that only certain resonances aside from the fundamental mode could be measured by electrical means, and that the only significantly non-zero one (i.e., the 4th mode) was unresponsive to changes in gas composition. The search for other orthogonal channels of data that could increase selectivity led back to the fundamental resonance. As is evident in Fig. 9a, the change in gas composition from Ar to N_2 to He causes large frequency shifts resulting from relative changes in the degree of inertial/viscous damping; the proof-of-concept experiments in FY10 which demonstrated selective gas detection were based entirely on these shifts in conjunction with the TCD sensor.

The reduction or increase in resonant frequency, depending on the change in damping relative to the reference condition, is well-known from the classical mechanics of damped oscillation. Although the flexural oscillations of a cantilever are not harmonic,[32] as is evident in the non-integral spacing of frequencies in Table 1, the displacement is often approximated using the classical damped oscillator equation. The degree of damping is typically expressed in terms of its temporal effect on the oscillation. If we define the time δt necessary for damping to reduce the oscillation amplitude by a factor e^{-1}, the frequency shift Δf in the fundamental mode is expressed:

$$\Delta f = f - f_0 = \sqrt{f_0^2 \pm \left(\frac{\delta f}{2\sqrt{2}\pi}\right)^2} - f_0 \qquad (1)$$

where δf is defined as the inverse of δt, and the plus/minus sign corresponds to negative/positive damping relative to the reference condition, respectively.[33] The maximum amplitude of flexural oscillation then depends on the damping through the quality factor $Q \equiv 2\pi f_0/\delta f$:

$$A_{max} = \frac{f_0 Q}{K\sqrt{1-(1/4Q^2)}} \qquad (2)$$

where K is the cantilever spring constant.[33] The corresponding full width at half maximum FWHM for the resonance peak is approximately equal to:[33]

$$\text{FWHM} \cong \frac{\sqrt{3}\delta f}{2\pi} \qquad (3)$$

Therefore, in addition to the frequency shift described by Eq. 1, there is an attenuation or amplification of the resonance peak height (Eq. 2) accompanied by a broadening or narrowing of the peak width (Eq. 3), respectively. For example, if the relative damping is reduced – such as when the gas environment is changed from N_2 to a less dense and viscous gas such as He – the damping time δt increases, δf decreases, and Q and A_{max} increase while the FWHM simultaneously decreases. The amplification and narrowing behavior with decreased damping, and the attenuation and broadening behavior with increased damping, for the fundamental resonance peak can be clearly observed in Fig. 9a.

To determine if gas selectivity could be increased by combining peak shape change information with the frequency shifts, we first had to determine a method for assessing the former data. Since we previously measured a single frequency shift, our first attempt at incorporating peak shape change was based on using two frequency shifts corresponding to the upper and lower frequencies bounding the FWHM (i.e., "half-peak" frequencies). In FY10, the selectivity of the gas leak sensor was demonstrated by combining the TCD sub-sensor output

with a single CFDRD data channel (peak frequency shift); here, the TCD data channel was combined with two CFDRD data channels (pair of "half-peak" frequency shifts). We used principal component analysis (PCA) to determine whether the additional channel of data, which effectively constitutes another sensing modality, is orthogonal to the other two data channels. PCA is widely utilized in the analysis of spectroscopic data, and has also been frequently applied to chemical detection data to help discern analyte signatures for multi-channel sensor arrays (see, for example, Refs. 34-36). The results of the comparative PCA analysis are shown below (Fig. 10). The incorporation of peak shape change produced a substantially measureable increase in selectivity, with the additional resolution of test gases (ultrahigh purity Ar and CO_2).

The limit of detection (LOD) for these data can be estimated using the smallest resolvable separation between clusters of gas data. In Fig. 10, each experimental data cluster was replaced by their mean value and a contour representing one standard deviation (1σ). As described in our previous work with chemical sensors, these contours define the effective noise in the system (gas leak sensor plus experimental apparatus).[34] We then computed the LOD based on a linear scaling

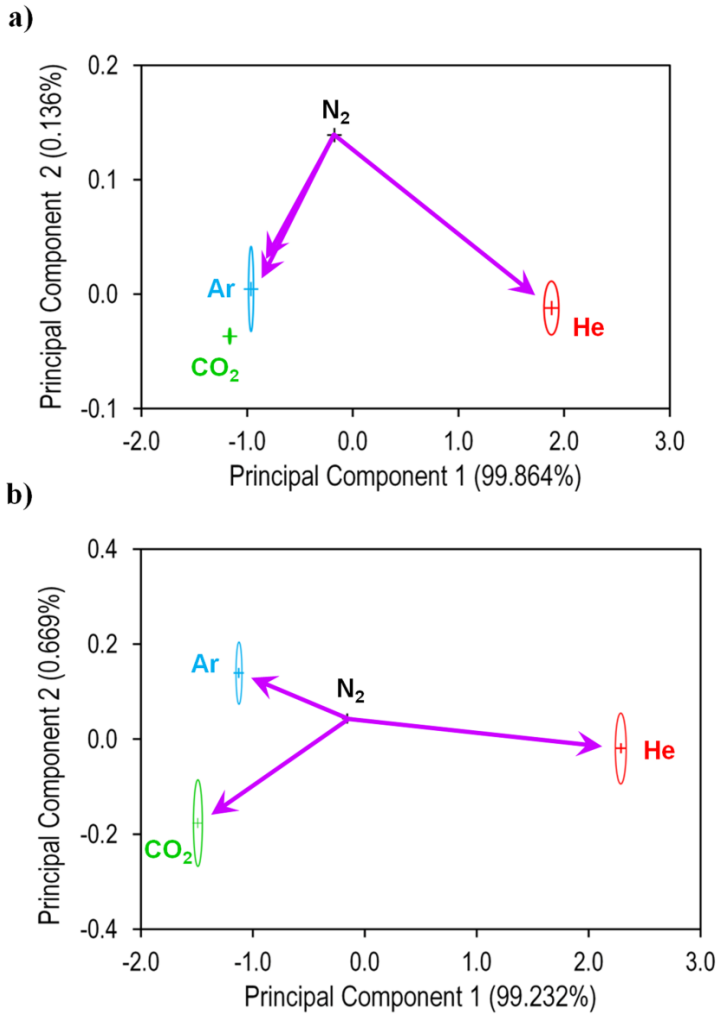

Figure 10. Two-dimensional PCA plots of combined TCD/CFDRD data for sensor exposure to ultrahigh purity test gases (N_2, Ar, CO_2, and He). a) TCD plus one CFDRD data channel. b) TCD plus two CFDRD data channels.

of the experimental responses to a value equivalent to a signal-to-noise ratio of three, a common practice in signal analysis. For the current breadboard-level sensor configuration, the LOD is thus found to be approximately 70 parts-per-thousand. As argued in Section 1.2.1, this level of sensitivity would permit the selective detection of a pressure-driven leak, such as one illustrated in Fig. 5, within a couple of hours. Given the crude level of circuit development, electrical sources of noise can certainly be reduced further. In addition, the successful implementation of a peak fitting algorithm, as discussed in Section 1.3.1, would effectively average out any residual noise. These strategies should improve the LOD and thereby expand the leak detection capabilities of the TCD/CFDRD sensor.

In practice, the incorporation of peak shape change using "half-peak" frequency shift may be difficult to implement. Since an absolute spectral baseline is difficult to define even after optimizing the peak for symmetry (Section 1.3.1), direct measurements of A_{max}, FWHM, and therefore the "half-peak" frequencies will be somewhat imprecise. The strategy described in the previous section – monitoring a sparse number of fixed frequencies and using a fitting function – will solve this problem; rather than follow a particular phase value (such as the "half-peak") as it shifts in the frequency domain, the changes in phase can be measured for each fixed frequency. For *n* fixed frequencies, this is equivalent to having *n* channels of data; however, the same peak shape change information is captured compared to monitoring the two "half-peak" frequencies, but without any of the aforementioned difficulties.

1.3.3 Thermal Drift Compensation

In Section 1.3.1, it was shown that the 4th resonant mode was intrinsically insensitive to changes in gas composition, making it an ideal candidate for the reference signal in a differential thermal drift compensation scheme. To qualify, the 4th mode must have the same thermally-induced frequency drift as the 1st mode, which carries the CFDRD sub-sensor signal. To measure the frequency drift as a function of temperature, the slope of which defines the temperature coefficient of frequency (TCF), we have designed a twin-chambered gas flow cell to be used in conjunction with a temperature-controlled heater. Schematic and technical drawings for the flow cell are shown in Appendix C. Each chamber of the cell contains a single TCD sub-sensor (modified Cantion CantiChip4) adjacent to a single CFDRD sub-sensor (Bruker Active Probe). Electrical connections to the commercial transducers are made via gold-plated pins (Mill-Max) affixed in a Delrin insulator plate and sealed with a vacuum-compatible epoxy resin (Loctite 1C Hysol or equivalent). Gas flow through each chamber is strictly regulated by digital mass flow controllers (Sierra Instruments C100), and only ultrahigh purity grade test gases will be used. The flow cell will be constructed from aluminum alloy for high thermal conductivity, and has a removable lid to allow installation and replacement of the sub-sensor transducers; the lid forms a gas-tight seal with each chamber using a pair of Viton O-rings. A miniature benchtop temperature controller (Omega CSi32) completes the experimental test apparatus. The 1st and 4th resonant modes can be alternately generated on the same Active Probe cantilever, with the latter mode insensitive to changes in the gas composition; as a result, both the sensor and reference signals can be generated from a single transducer residing within the test gas. However, the TCD sub-sensor transducer is physically distinct from its reference, which is identical within manufacturing tolerances but operates on the exact same principle (i.e., heat dissipation). As a result, the TCD sub-sensor and its reference must reside in separate environments containing the

test gas and reference gas, respectively. The two separate chambers of the flow cell satisfy this requirement.

The final design was completed in mid-Q4/FY11, and DV Manufacturing, Inc (Livermore, CA) agreed in principle to fabricate and assemble the gas flow cell. However, a combination of circumstances delayed the formal procurement process until the start of FY12: 1) the vendor, which services many clients at federally-funded research and development centers like LLNL, had a backlog of projects through the end of FY11; 2) one of the vendor's chief welders was on extended leave during the month of September; 3) the project account was effectively frozen for procurements during the final two weeks of FY11, as normally mandated by LLNL Supply Chain Management. Barring production difficulties, the current estimated delivery date is early November 2012.

1.4 Conclusion

In Fiscal Year 2011, we made several advances in the research and development of a non-spectroscopic method for noble gas leak detection, specifically in the coating-free damped resonance detection sub-system. Improvements to the circuitry and instrumentation allowed multiple normal modes to be excited and read out, enabling the discovery of a resonance (the 4^{th} mode) that is insensitive to changes in the gas composition and opening the way for thermal drift compensation without a secondary reference sensor. While the search for higher resonances orthogonal to the fundamental mode ultimately proved fruitless, it inspired a similar search within the mechanical aspects of the fundamental resonance itself. The recognition that the peak shape change is effectively orthogonal to the frequency shift during changes in gas composition, and the incorporation of the latter effect into the sensor response, led directly to the increased selectivity for the TCD/CFDRD gas leak sensor. Initial efforts in moving from high frequency resolution scans of the resonance peak, to a cyclic monitoring of a sparse number of fixed frequencies combined with functional fits, will pave the way for improvements in the speed and efficiency of the data acquisition process. Finally, an experimental test apparatus was designed to investigate the aforementioned thermal drift behavior and measure the TCF for the 1^{st} and 4^{th} normal modes.

In FY12, the project will continue with thermal testing of the apparatus (Q1), with the goal of demonstrating thermal drift compensation in both the CFDRD and TCD sensor sub-systems. Challenge testing with simulated pre- and post-leak gas environments is planned for the duration of Q2. Since FY11 was focused on advancing the state of the CFDRD method, efforts will be made to replace the current TCD sub-sensor (a research grade piezoresistive microcantilever array) with a mass-produced precision thermistor (Q3). Once final selection of the TCD sub-sensor is made, we will begin the task of sensor head integration (Q4).

This work was performed under the auspices of the U.S. Department of Energy by Lawrence Livermore National Laboratory under Contract DE-AC52-07NA27344.

1.5 References

[1] J. R. Brown, S. M. Thornberg, J. F. Banet, L. Woods, and J. Ithaca, Sandia National Laboratories Report No. SAND2006-2845, 2006.
[2] H. Hoffmeister, Nucl. Eng. Des. **239**, 1795 (2009).
[3] A. Turnbull, Corrosion Sci. **39**, 789 (1997).
[4] M. E. Hoffman and P. C. Hoffman, Int. J. Fatigue **23**, S1 (2001).
[5] A. Loui, D. J. Sirbuly, S. Elhadj, S. K. McCall, B. R. Hart, and T. V. Ratto, Sens. Actuators A **159**, 58 (2010).
[6] L. A. Pinnaduwage, A. Wig, D. L. Hedden, A. Gehl, D. Yi, T. Thundat, and R. T. Lareau, J. Appl. Phys. **95**, 5871 (2004).
[7] J. D. Adams, G. Parrott, C. Bauer, T. Sant, L. Manning, M. Jones, B. Rogers, D. McCorkle, and T. L. Ferrell, Appl. Phys. Lett. **83**, 3428 (2003).
[8] I. Voiculescu, M. Zaghloul, R. A. McGill, E. J. Houser, and G. K. Fedder, IEEE Sens. J. **5**, 641 (2005).
[9] A. Biedermann, E. Knoesel, Z. Hu, and T. F. Heinz, Phys. Rev. Lett. **83**, 1810 (1999).
[10] K. D. Rendulic, Surf. Sci. **272**, 34 (1992).
[11] G. Ertl, S. B. Lee, and M. Weiss, Surf. Sci. **114**, 515 (1982).
[12] K. Walter, *A Better Picture of Aging Materials*, in Science & Technology Review (Lawrence Livermore National Laboratory), Sept. 1999, p. 4.
[13] M. A. Henderson, Surf. Sci. Rep. **46**, 5 (2002).
[14] NIST Chemistry WebBook: http://webbook.nist.gov/chemistry/.
[15] C. Dücső, M. Ádám, P. Fürjes, M. Hirschfelder, S. Kulinyi, and I. Bársony, Sens. Actuator B **95**, 189 (2003).
[16] I. Simon and M. Arndt, Sens. Actuators A **97-98**, 104 (2001).
[17] G. Pollak-Diener and E. Obermeier, Sens. Actuators B **13**, 345 (1993).
[18] S. Tetin, B. Caillard, F. Menil, H. Debeda, C. Lucat, C. Pellet, and I. Dufour, Sens. Actuator B-Chem. **143**, 555 (2010).
[19] Y. Xu, J. T. Lin, B. W. Alphenaar, and R. S. Keynton, Appl. Phys. Lett. **88**, 143513 (2006).
[20] R. Block, G. Fickler, G. Lindner, H. Muller, and M. Wohnhas, Sens. Actuator B-Chem. **7**, 596 (1992).
[21] A. Kurokawa, H. Hojo, and T. Kobayashi, Appl. Phys. Express **4**, 3 (2011).
[22] J. K. Sell, A. O. Niedermayer, S. Babik, and B. Jakoby, Sens. Actuator A-Phys. **162**, 215 (2010).
[23] D. Zeisel, H. Menzi, and L. Ullrich, Sens. Actuator A-Phys. **80**, 233 (2000).
[24] J. Kehrbusch, E. A. Ilin, P. Bozek, B. Radzio, and E. Oesterschulze, Sci. Technol. Adv. Mater. **10**, 034601 (2009).
[25] Bruker AFM Probes: http://www.brukerafmprobes.com.
[26] NANOSENSORS AFM probes: http://www.akiyamaprobe.com.
[27] S. N. Mahmoodi, N. Jalili, and M. Ahmadian, Nonlinear Dyn. **59**, 397 (2010).
[28] A. Salehi-Khojin, S. Bashash, and N. Jalili, J. Micromech. Microeng. **18**, 11 (2008).
[29] P. Sanz, J. Hernando, J. Vazquez, and J. L. Sanchez-Rojas, J. Micromech. Microeng. **17**, 931 (2007).
[30] ANSI/IEEE, *IEEE Standard on Piezoelectricity (withdrawn)*, Std 176-1987 (1988).
[31] K. Naeli and O. Brand, Rev. Sci. Instrum. **80**, 8 (2009).
[32] O. Sahin, C. F. Quate, O. Solgaard, and A. Atalar, Phys. Rev. B **69**, 9 (2004).
[33] G. Y. Chen, R. J. Warmack, T. Thundat, D. P. Allison, and A. Huang, Rev. Sci. Instrum. **65**, 2532 (1994).
[34] A. Loui, T. V. Ratto, T. S. Wilson, S. K. McCall, E. V. Mukerjee, and B. R. Hart, Analyst **133**, 608 (2008).
[35] N. S. Lewis, Acc. Chem. Res. **37**, 663 (2004).
[36] M. K. Baller, et al., **82**, 1 (2000).
[37] Handbook of Chemical Hazard Analysis Procedures, U.S. Federal Emergency Management Agency, U.S. Department of Transportation, U.S. Environmental Protection Agency, 1989.

[38] R. H. Perry and D. W. Green, *Perry's Chemical Engineers' Handbook (7th edition)* (McGraw-Hill, New York, 1997).
[39] F. Rasouli and T. A. Williams, J. Air Waste Manage. Assoc. **45**, 191 (1995).
[40] D. Peng and D. B. Robinson, Ind. Eng. Chem. Fundam. **15**, 59 (1976).
[41] K. S. Pitzer, D. Z. Lippmann, R. F. Curl, C. M. Huggins, and D. E. Petersen, J. Am. Chem. Soc. **77**, 3433 (1955).
[42] U. K. Deiters, Aiche J. **48**, 882 (2002).
[43] W. Ranke, Surf. Sci. **369**, 137 (1996).
[44] W. Ranke and D. Schmeisser, Surf. Sci. **149**, 485 (1985).
[45] NIST Reference on Constants, Units, and Uncertainty: http://physics.nist.gov/CUU/Constants/index.html.
[46] W. Ranke and Y. R. Xing, Surf. Sci. **157**, 339 (1985).
[47] NOAA National Weather Service: http://weather.gov.
[48] A. L. Buck, J. Appl. Meteorol. **20**, 1527 (1981).
[49] D. P. Woodruff and T. A. Delchar, *Modern Techniques of Surface Science (2nd edition)* (Cambridge University Press, New York, 1994).
[50] G. Y. Chen, T. Thundat, E. A. Wachter, and R. J. Warmack, **77**, 3618 (1995).

Appendix A: Modeling of a Pressure-Driven Gas Leak

Consider two contiguous containment vessels 1 and 2, filled with gases at pressures P_1 and P_2, respectively. A breach occurs in the adjoining wall; if $P_1 > P_2$, the gas within vessel 1 will leak into vessel 2 until the pressure in each vessel is equal. Once a steady-state is reached, advection ceases and interdiffusion of the gases will occur slowly under isobaric conditions until the gas composition in both vessels is homogeneous.

We begin by assuming that the leaking gas flow is inviscid, incompressible, and laminar – that is, characterized by zero viscosity (i.e., no frictional losses), constant mass density, and an absence of turbulence, respectively. The conservation of energy per unit volume for gas flow from vessel 1 into the breach is simply stated by the Bernoulli equation:

$$\mathrm{P}_1 = \mathrm{P}_b + \frac{\rho v_b^2}{2} \tag{1}$$

where ρ is the mass density and the subscript "b" denotes the conditions within the breach; note that a translational kinetic energy density term is absent from the left-hand side of the equation, since the gas is initially stationary in vessel 1. Using the definition of volumetric flow Q, Eq. 1 can be rearranged to give

$$P_1 = P_b + \left(\frac{\rho}{2}\right)\left(\frac{Q}{A_b}\right)^2$$

$$Q = A_b\sqrt{\frac{2(P_1 - P_b)}{\rho}} \tag{2}$$

where A_b is the cross-sectional area of the breach. The mass flow rate $\dot{m}$ is then given by the product of ρ and Q:

$$\dot{m} \equiv \frac{dm}{dt} = \rho Q = A_b\sqrt{2\rho(P_1 - P_b)} \tag{3}$$

From Eq. 1, it is evident that the pressure P_b of the gas moving within the breach is reduced relative to the upstream pressure P_1; however, since $P_1 > P_2$ and the gas within vessel 2 is also stationary (i.e., the leaking gas comes to rest), the conservation of energy requires that some energy per unit volume was lost within the breach. Such losses can be attributed to the effects of turbulence at the entrance and exit openings of the breach, as well as friction within the breach. In addition gases, compared to condensed states of matter, are readily compressible or expandable; as such, $\dot{m}$ must be appropriately modified to account for changes in density. We replace P_b with the more convenient downstream pressure P_2, reinterpret ρ as the upstream density, and capture all of the aforementioned phenomena in two factors – a flow coefficient C and an expansion factor Y:

$$\dot{m} = CYA_b\sqrt{2\rho(P_1 - P_2)} \tag{4}$$

Pressure-driven leaks are typically considered isentropic processes, where the gas expands adiabatically through the breach and does positive work on the gas beyond; for example, this assumption is incorporated into the Automated Resource for Chemical Hazard Incident Evaluation (ARCHIE) computational model employed by several U.S. federal agencies, allowing the prediction of accidental gas release into the environment.[37] For breaches much smaller than the dimensions of the containment vessels, the isentropic expansion factor is approximately given by

$$Y \cong \sqrt{\left(\frac{P_2}{P_1}\right)^{\frac{2}{\gamma}}\left(\frac{\gamma}{\gamma-1}\right)\left[\frac{1-\left(\frac{P_2}{P_1}\right)^{\frac{\gamma-1}{\gamma}}}{1-\left(\frac{P_2}{P_1}\right)}\right]} \tag{5}$$

where γ is the well-known ratio of heat capacity at constant pressure C_p to heat capacity at constant volume C_v.[38] Substituting this expression into Eq. 4 and simplifying:

$$\dot{m} = CA_b\sqrt{\left(\frac{\gamma}{\gamma-1}\right)\left[\frac{\left(\frac{P_2}{P_1}\right)^{\frac{2}{\gamma}}-\left(\frac{P_2}{P_1}\right)^{\frac{\gamma+1}{\gamma}}}{\frac{(P_1-P_2)}{P_1}}\right]\sqrt{2\rho(P_1-P_2)}}$$

$$\dot{m} = CA_b\sqrt{2\rho P_1\left(\frac{\gamma}{\gamma-1}\right)\left[\left(\frac{P_2}{P_1}\right)^{\frac{2}{\gamma}}-\left(\frac{P_2}{P_1}\right)^{\frac{\gamma+1}{\gamma}}\right]}$$

In general, the upstream pressure P_1 may be much larger than the ambient atmospheric pressure (nominally 14.7 psia) and possibly approach or exceed the critical pressure value for gas 1; thus, departures from ideal gas behavior should be accounted using the compressibility factor *Z*. Using the definitions for *Z* and density, the mass flow rate expression becomes:

$$\dot{m} = CA_b\sqrt{2\left(\frac{P_1M_1}{ZRT}\right)P_1\left(\frac{\gamma}{\gamma-1}\right)\left[\left(\frac{P_2}{P_1}\right)^{\frac{2}{\gamma}}-\left(\frac{P_2}{P_1}\right)^{\frac{\gamma+1}{\gamma}}\right]}$$

$$\dot{m} = CA_bP_1\sqrt{\left(\frac{2M_1}{ZRT}\right)\left(\frac{\gamma}{\gamma-1}\right)\left[\left(\frac{P_2}{P_1}\right)^{\frac{2}{\gamma}}-\left(\frac{P_2}{P_1}\right)^{\frac{\gamma+1}{\gamma}}\right]} \tag{6}$$

where M_1 is the molecular mass of gas 1, *R* is the ideal gas constant, and *T* is the upstream gas temperature. The volumetric flow rate *Q* can be recovered by dividing Eq. 6 by the density

$$Q = CA_b\sqrt{\left(\frac{2ZRT}{M_1}\right)\left(\frac{\gamma}{\gamma-1}\right)\left[\left(\frac{P_2}{P_1}\right)^{\frac{2}{\gamma}}-\left(\frac{P_2}{P_1}\right)^{\frac{\gamma+1}{\gamma}}\right]} \tag{7}$$

while the speed of the gas v_b within the breach is obtained by dividing *Q* by the effective cross sectional area $A_b' \equiv C'A_b$, where the discharge coefficient C' accounts for the contraction of leak flow at the entrance to the breach (i.e., vena contracta):[38]

$$v_b = \frac{C}{C'}\sqrt{\left(\frac{2ZRT}{M_1}\right)\left(\frac{\gamma}{\gamma-1}\right)\left[\left(\frac{P_2}{P_1}\right)^{\frac{2}{\gamma}}-\left(\frac{P_2}{P_1}\right)^{\frac{\gamma+1}{\gamma}}\right]} \tag{8}$$

Intuitively, v_b should increase as the pressure differential between the contiguous containment vessels increases – that is, as $P_1–P_2$ (or, alternatively, P_1/P_2) grows in magnitude. However, in the limit $P_1/P_2 \rightarrow \infty$, Eq. 8 approaches an indeterminate form. To determine the maximum value of v_b as a function of P_1/P_2, let *x* equal the ratio of pressures and set the derivative of Eq. 8 with respect to *x* equal to zero:

$$\frac{\partial v_b}{\partial x} = \frac{\frac{C}{2C'}\left(\frac{2ZRT}{M_1}\right)\left(\frac{\gamma}{\gamma-1}\right)\left[-\frac{2}{\gamma}x^{-\frac{2}{\gamma}-1}+\left(\frac{\gamma+1}{\gamma}\right)x^{-\frac{\gamma+1}{\gamma}-1}\right]}{\sqrt{\left(\frac{2ZRT}{M_1}\right)\left(\frac{\gamma}{\gamma-1}\right)\left(x^{-\frac{2}{\gamma}}-x^{-\frac{\gamma+1}{\gamma}}\right)}} = 0$$

$$\frac{2}{\gamma}x^{-\frac{2}{\gamma}-1} = \left(\frac{\gamma+1}{\gamma}\right)x^{-\frac{\gamma+1}{\gamma}-1}$$

$$x^{-\frac{2+\gamma}{\gamma}} = \frac{\gamma+1}{2}x^{-\frac{2\gamma+1}{\gamma}}$$

$$x^{\frac{\gamma-1}{\gamma}} = \frac{\gamma+1}{2}$$

Therefore, the maximum value of v_b is attained when the ratio of pressures $x \equiv P_1/P_2$ satisfies the condition

$$\frac{P_1}{P_2} = \left(\frac{\gamma+1}{2}\right)^{\frac{\gamma}{\gamma-1}} \tag{9}$$

Substituting Eq. 9 into Eq. 8, we obtain an expression for the maximum gas leak speed:

$$v_{b,max} = \frac{C}{C'}\sqrt{\left(\frac{2ZRT}{M_1}\right)\left(\frac{\gamma}{\gamma-1}\right)\left\{\left[\left(\frac{2}{\gamma+1}\right)^{\frac{\gamma}{\gamma-1}}\right]^{\frac{2}{\gamma}}-\left[\left(\frac{2}{\gamma+1}\right)^{\frac{\gamma}{\gamma-1}}\right]^{\frac{\gamma+1}{\gamma}}\right\}}$$

$$v_{b,max} = \frac{C}{C'}\sqrt{\left(\frac{2ZRT}{M_1}\right)\left(\frac{\gamma}{\gamma-1}\right)\left(\frac{2}{\gamma+1}\right)^{\frac{\gamma+1}{\gamma-1}}\left[\left(\frac{2}{\gamma+1}\right)^{\frac{1-\gamma}{\gamma-1}}-1\right]}$$

$$v_{b,max} = \frac{C}{C'}\sqrt{\left(\frac{2ZRT}{M_1}\right)\left(\frac{\gamma}{\gamma-1}\right)\left(\frac{2}{\gamma+1}\right)^{\frac{\gamma+1}{\gamma-1}}\left(\frac{\gamma+1}{2}-1\right)}$$

$$v_{b,max} = \frac{C}{C'}\sqrt{\left(\frac{\gamma ZRT}{M_1}\right)\left(\frac{2}{\gamma+1}\right)^{\frac{\gamma+1}{\gamma-1}}} \tag{10}$$

The phenomenon described above is commonly known as choked flow, where the gas speed through a breach or orifice attains a fixed maximum value as long as the ratio of upstream and downstream pressures equals or exceeds the value given by Eq. 9. This maximum speed can be shown to equal the speed of sound a for gas 1 at temperature T, which is given by the well-known thermodynamic expression[38]

$$a = \sqrt{\left(\frac{\gamma ZRT}{M_1}\right)} \tag{11}$$

By comparing Eqs. 10 and 11, we obtain a value for the ratio of flow and discharge coefficients:

$$\frac{C}{C'} = \left(\frac{\gamma+1}{2}\right)^{\frac{\gamma+1}{2(\gamma-1)}} \tag{12}$$

The discharge coefficient C' typically takes on values between 0.60 and 0.70;[38] assuming an ideal value of 0.611 corresponding to a perfectly sharp-edged circular orifice, the flow coefficient can then be obtained from Eq. 12. The mass flow rate in the choked condition can be derived by substituting Eqs. 9 and 12 into Eq. 6:

$$\dot{m}_{choked} = CA_b P_1 \sqrt{\left(\frac{2M_1}{ZRT}\right)\left(\frac{\gamma}{\gamma-1}\right)\left\{\left[\left(\frac{2}{\gamma+1}\right)^{\frac{\gamma}{\gamma-1}}\right]^{\frac{2}{\gamma}} - \left[\left(\frac{2}{\gamma+1}\right)^{\frac{\gamma}{\gamma-1}}\right]^{\frac{\gamma+1}{\gamma}}\right\}}$$

$$\dot{m}_{choked} = CA_b P_1 \sqrt{\left(\frac{2M_1}{ZRT}\right)\left(\frac{\gamma}{\gamma-1}\right)\left(\frac{2}{\gamma+1}\right)^{\frac{\gamma+1}{\gamma-1}}\left[\left(\frac{2}{\gamma+1}\right)^{\frac{1-\gamma}{\gamma-1}} - 1\right]}$$

$$\dot{m}_{choked} = CA_b P_1 \sqrt{\left(\frac{2M_1}{ZRT}\right)\left(\frac{\gamma}{\gamma-1}\right)\left(\frac{2}{\gamma+1}\right)^{\frac{\gamma+1}{\gamma-1}}\left(\frac{\gamma+1}{2} - 1\right)}$$

$$\dot{m}_{choked} = CA_b P_1 \sqrt{\left(\frac{\gamma M_1}{ZRT}\right)\left(\frac{2}{\gamma+1}\right)^{\frac{\gamma+1}{\gamma-1}}}$$

$$\dot{m}_{choked} = C' A_b P_1 \sqrt{\left(\frac{\gamma M_1}{ZRT}\right)} \tag{13}$$

It should be evident that, while the gas leak speed is equal to the sonic speed in the choked condition, the mass flow rate can be increased in direct proportion to the upstream pressure P_1 only; once P_1 falls below the threshold value given by Eq. 9, v_b becomes subsonic and the mass flow once again depends on both the upstream and downstream pressures (Eq. 6).

The temporal evolution of a pressure-driven gas leak as a function of breach size must be computed iteratively, since the pressure in vessel 1 diminishes in time while the pressure in vessel 2 increases correspondingly; the mass flow rate will decrease continuously until $P_1 = P_2$, at which point $\dot{m}$ will fall to zero. In typical environmental release scenarios, a single containment vessel leaks gas into the ambient atmosphere (see, for example, Ref. 39); in this case, the environmental "vessel" is so large that the added gas is negligible and the downstream pressure remains constant (e.g., 14.7 psia). In the present example, both P_1 and P_2 must be modified at each time step in the calculation. The iterative computational procedure is described below:

a) Calculate C_p at the initial upstream temperature T using the empirical Shomate equation;[14] it is assumed that the gas in each vessel is equilibrated at this temperature initially.
b) Using C_p and $C_v = C_p – R$, calculate γ.
c) Using γ, calculate the threshold value for choked flow using Eq. 9 and the initial values for P_1 and P_2.
d) Compute $Z(P,T)$ using the Peng-Robinson equation of state;[40] this empirical expression depends on several parameters:
    i) The critical pressure P_c and temperature T_c,[14] above which the liquid/gas phase boundary vanishes;
    ii) The acentric factor ω, which depends on P_c and T_c and addresses the oversimplified assumption of idealized point-like particles in the ideal gas law;[41]

    The expression for Z is a cubic equation, which can be solved using Cardano's method;[42] in the event that there is more than one real root, the larger root corresponds to the compressibility factor for the gas phase.

e) Compute $\dot{m}$ using γ, Z, M_1, and gas state variables for a breach of cross-sectional area A_b. If P_1 exceeds the threshold value for choked flow, compute the mass flow rate using Eq. 13; otherwise, use Eq. 6.

f) Using the Peng-Robinson equation of state,[40] compute the number of gas particles N_1 and N_2 in vessels 1 and 2, respectively:

$$N = \left(\frac{PV}{ZRT}\right) N_A \tag{14}$$

where N_A is Avogadro's number.

g) Determine the particle flow rate $\partial N_1/\partial t$ using $\dot{m}$:

$$\frac{\partial N_1}{\partial t} = \dot{m}\left(\frac{N_A}{M_1}\right) \tag{15}$$

h) For a sufficiently small time step δt, compute the number of gas particles which has leaked from vessel 1 to vessel 2.

i) Using the Peng-Robinson equation of state,[40] calculate the new pressure values for vessels 1 and 2:

$$P = \left(\frac{N \pm \frac{\partial N_1}{\partial t}\delta t}{N_A}\right)\left(\frac{ZRT}{V}\right) \tag{16}$$

where the plus and minus signs correspond to vessels 2 and 1, respectively.

j) Under the original isentropic assumption, the internal energy of the leaking gas is reduced as it expands adiabatically through the breach and does positive work on the gas beyond; thus, the gas in vessel 1 will cool according to the thermodynamic relation:[38]

$$T(t+\delta t) = T(t)\left[\frac{P_1(t+\delta t)}{P_1(t)}\right]^{\frac{\gamma-1}{\gamma}} \tag{17}$$

k) Repeat Steps a through j until $P_1 = P_2$; calculations of $\dot{m}$ and v_b using Eqs. 6 and 8 (respectively) should both yield values of zero in this condition.

One caveat with the pressure-driven gas leak model is that the isentropic condition is most valid for rapid leaks associated with large breaches and pressure differentials, such that the timescale of non-zero leak rates is short and the implied adiabatic condition is most likely to be satisfied. For relatively slower leaks, it is more likely that considerable heat flow into the leaking vessel will occur, reducing or eliminating the cooling effect described by Eq. 17. If T is assumed to be relatively constant, the pressure P_1 will remain elevated compared to the strict isentropic condition since the temperature will be relatively higher; the overall effect is that the time evolution of the leak will be slower in the isothermal vs. the isentropic case. The actual temporal behavior of the leak will therefore lie somewhere between these two limiting conditions.

Appendix B: Estimating Resonant Damping from Vapor Sorption

Consider a silicon microcantilever at room temperature (20°C), the surface of which is completely devoid of adsorbed chemical species. In this ideally clean state, the cantilever will have a fundamental resonance frequency $f_{0,v}$ in a vacuum, and a reduced value f_0 in a fluid environment (gas, liquid, or supercritical fluid) where the relative degree of damping depends on the density and viscosity of the surrounding medium. Further suppose that the fluid is a perfectly inert gas, with no propensity to adhere or otherwise react with the bare cantilever surface (i.e., sticking coefficient $S = 0$). It is instructive to consider what happens when a common chemical vapor such as water is introduced into the gas. Will this water vapor adsorb onto the silicon cantilever surface ($S \neq 0$)? If so, any mass uptake by sorption will cause f_0 to decrease to a new value $f_{0,ads}$; in such a case, can we estimate the frequency shift $f_{0,ads} - f_0$?

The adsorption of water on silicon surfaces has been studied extensively under the controlled conditions of ultrahigh vacuum (see Ref. 13 and citations therein). For example, Ranke and co-workers used valence-band photoemission spectroscopy to show that water adsorbs to saturation coverage θ_{sat} = 0.5 monolayer (ML) at room temperature on the Si(001) surface, with multilayer formation onset below ~140K;[43, 44] such a low Miller index surface is also representative of a silicon microcantilever fabricated from a typical single-crystal Si (SCS) wafer. The adsorbate surface density σ_{sat} corresponding to θ_{sat} can be readily calculated. First, the atomic surface density σ can be determined from the diamond cubic structure of SCS, where a single 2-D unit cell for the Si(001) surface measures 5.43 Å × 5.43 Å and contains 2 atoms.[45] The sticking coefficient for water on Si(001) at room temperature is $S_w \cong 1$ for coverages from zero up to saturation.[43, 46] Combining this information leads to a value $\sigma_{sat} = 1*0.5*[2/(5.43\ \text{Å})^2] = 3.39\times10^{18}\ \text{m}^{-2}$.

Given sufficient time, any non-zero partial pressure of water vapor will deliver enough gaseous flux to the cantilever surface to achieve θ_{sat}. This concept of exposure is best illustrated with some realistic values. As an example, consider the ambient relative humidity RH = 30% and barometric pressure P = 29.90 inHg at T = 88°F in Livermore, CA during the late afternoon of September 29, 2011.[47] The saturation partial pressure of water vapor in air with respect to liquid water e'_w can be calculated using the empirical formula of Buck, which has an absolute error value of 0.20% in the -20°C to 50°C range:

$$e'_w = [1.0007 + (3.46 \times 10^{-6})P](6.1121)\exp\left(\frac{17.502T}{240.97+T}\right) \quad (1)$$

where P is given in hPa and T in degrees Celsius.[48] Substituting the weather data into Eq. 1 after converting units, we obtain the saturation value of 45.41 hPa or an actual partial pressure e_w = 0.30(45.41 hPa) = 13.62 hPa. To compute the amount of time needed to reach the adsorption saturation coverage, the corresponding surface density must be divided by the gaseous flux impinging upon the cantilever surface. The water vapor flux r_w is obtained by considering the fraction of randomly-moving gas molecules that are in proximity to the surface and which strike the surface per unit time; the integral expression for the expectation value of speed using the Maxwell-Boltzmann probability density function leads to the equation:

$$r_w = e_w\sqrt{\frac{1}{2\pi kTm}} \quad (2)$$

where k is the Boltzmann constant and m is the molecular mass.[49] Using the calculated value for e_w, Eq. 2 yields an impinging flux $r_w = 4.847\times10^{25}$ $m^{-2}s^{-1}$ and the corresponding exposure time to go from the clean to saturated condition is $t = \sigma_{sat}/r_w \cong 70$ ns. Therefore, the exposure of a silicon surface to typical ambient quantities of water vapor at room temperature will result in practically instantaneous sub-monolayer saturation.

For a monolithic cantilever, the post-adsorption resonant frequency $f_{0,ads}$ is approximately related to the pre-adsorption resonant frequency f_0 via the relation:

$$f_{0,\text{ads}} \cong f_0\left[1 - \frac{1}{2}\left(\frac{\delta m}{m_c^*}\right)\right] \tag{3}$$

where m_c^* is the effective cantilever mass and δm is the total mass added by adsorption;[50] we have excluded the possibility of adsorption-induced changes in cantilever stiffness, as described by Chen et al., since no differential surface stress should develop in the absence of a chemically-functional coating. We apply Eq. 3 to the commercial resonating cantilever (Bruker Active Probe) currently used in this project (Section 1.3.1). Although the commercial cantilever has a non-constant and non-linearly varying width, we estimate that the resulting value of m_c^* should be intermediate between typical V-shaped and purely rectangular planform designs; for these prototypical shapes, the effective cantilever mass lies in the range $0.13m_c \leq m_c^* \leq 0.24m_c$, where m_c is the actual cantilever mass.[33] The cantilever mass m_c (2.22×10^{-9} kg) is estimated based on the dimensions listed in the vendor specifications[25] and shown in Ref. 27, which allows the internal cantilever volume (5.63×10^{-13} m^3) to be computed. Using the same dimensions, the total surface area (1.99×10^{-7} m^2) can also be computed and, when multiplied by σ_{sat}, gives the total number of adsorbed water molecules which can be easily converted via the molar mass and Avogadro's number to δm (4.03×10^{-14} kg). With an average measured f_0 = 57.390 kHz, the resulting frequency shift $f_{0,ads} - f_0$ for a 0.5 ML saturation coverage of water vapor at 20°C is about -0.2 to -0.4 Hz.

Appendix C: Twin-Chambered Gas Flow Cell

Schematic and technical drawings for the twin-chambered gas flow cell, to be used for thermal drift testing, are attached on the following pages:

Twin-Chambered Gas Flow Cell for Sensor Thermal Testing

Albert Loui (loui2@llnl.gov)
(925) 422-2840
8/8/11

Exploded *Front* View

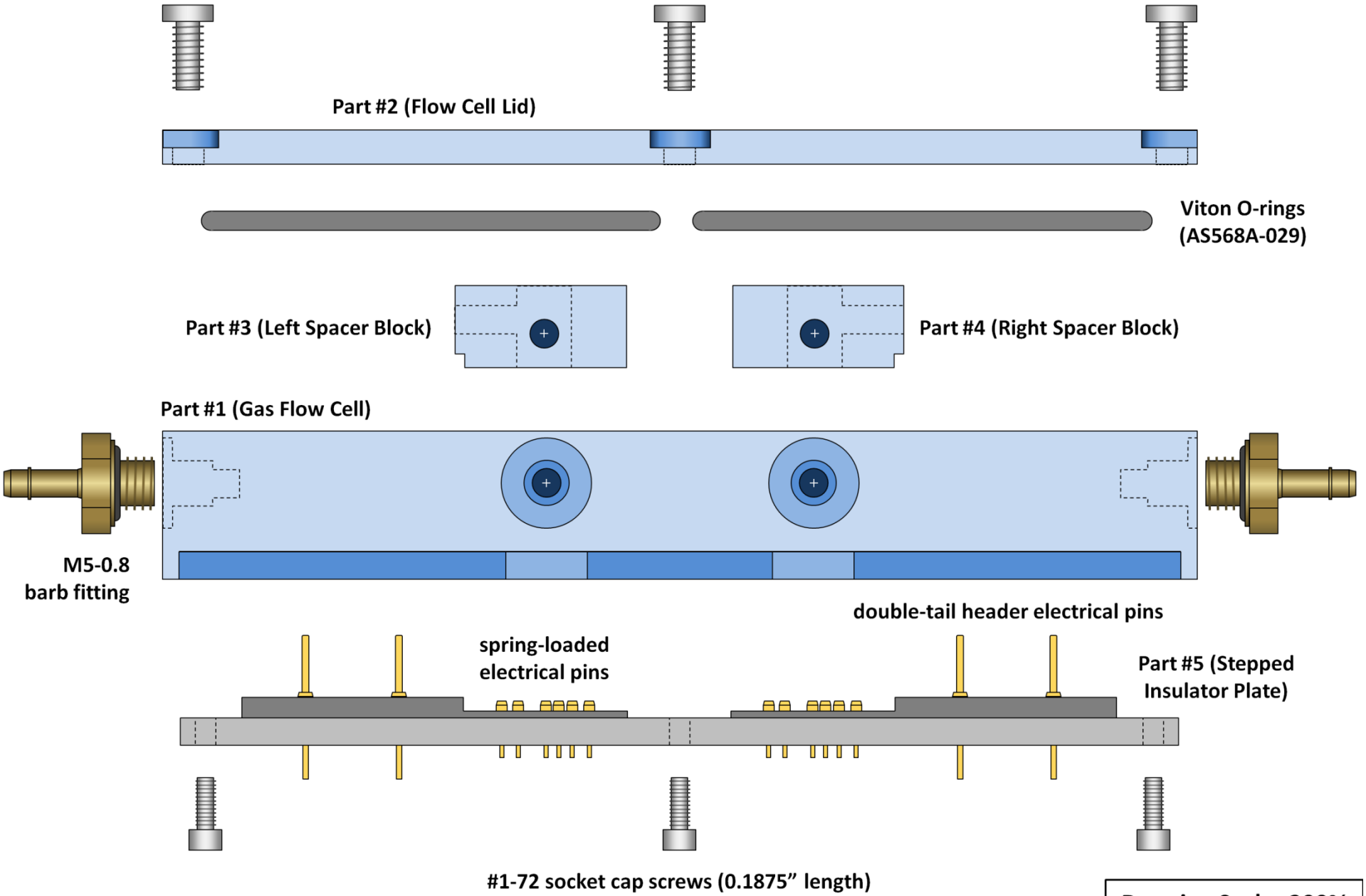

Drawing Scale: 200%

5) Stepped Insulator Plate (with electrical contact pins installed)

Albert Loui (loui2@llnl.gov)
(925) 422-2840
8/8/11

Schematic *Bottom* View

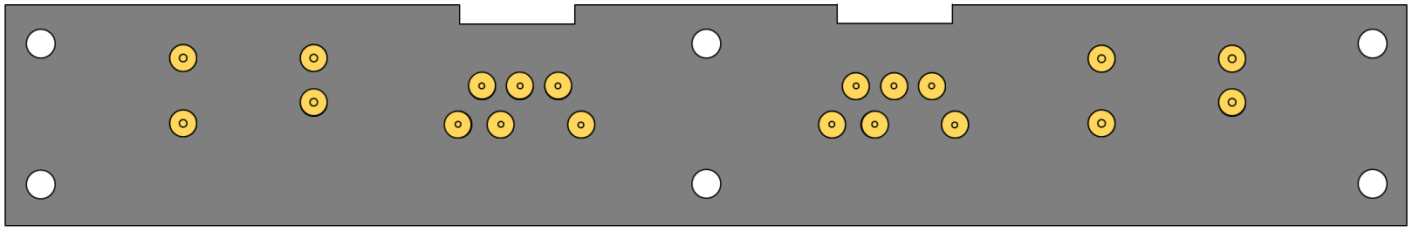

Schematic *Top* View

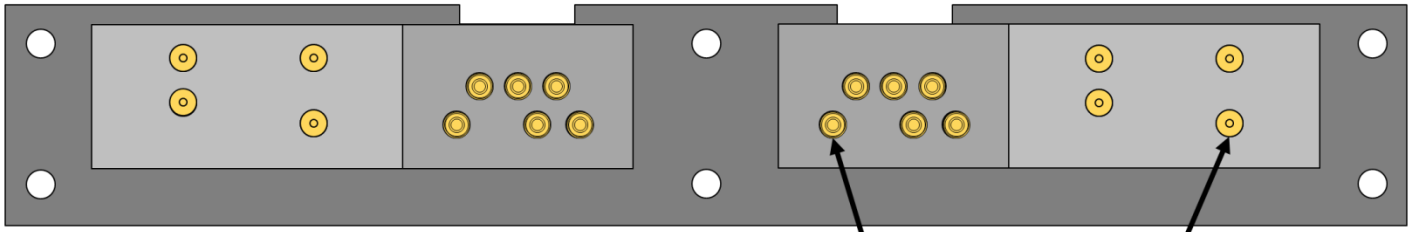

Schematic *Front* View

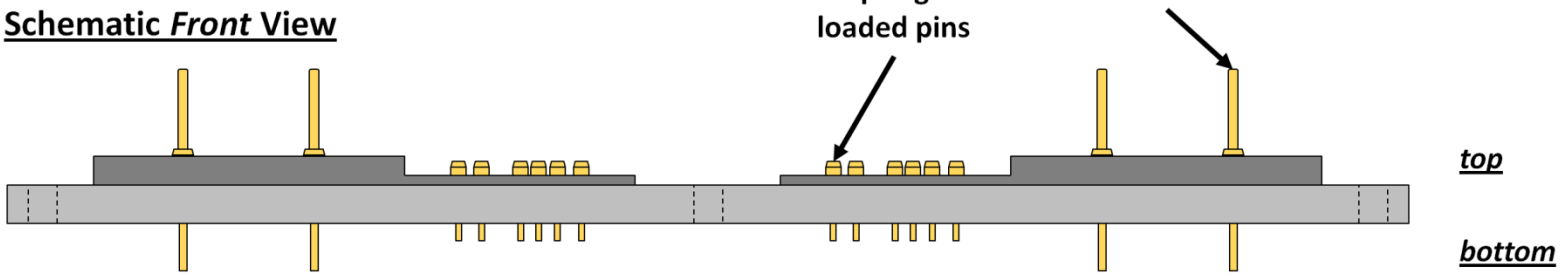

Drawing Scale: 200%

5) Stepped Insulator Plate (with electrical contact pins installed)

Albert Loui (loui2@llnl.gov)
(925) 422-2840
8/8/11

Schematic *Bottom* View

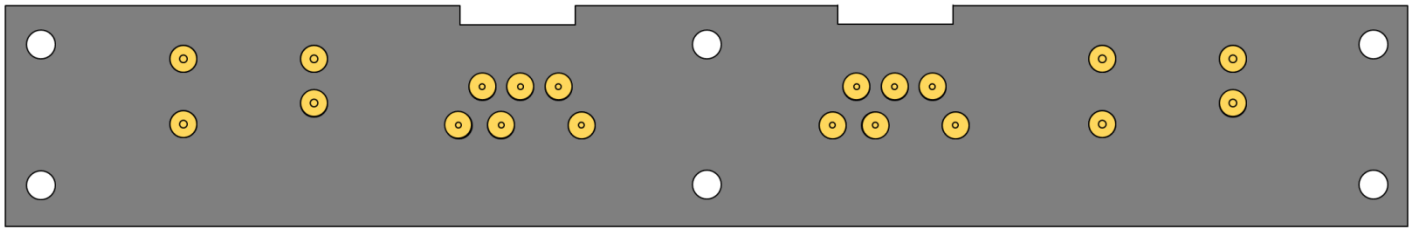

Schematic *Top* View

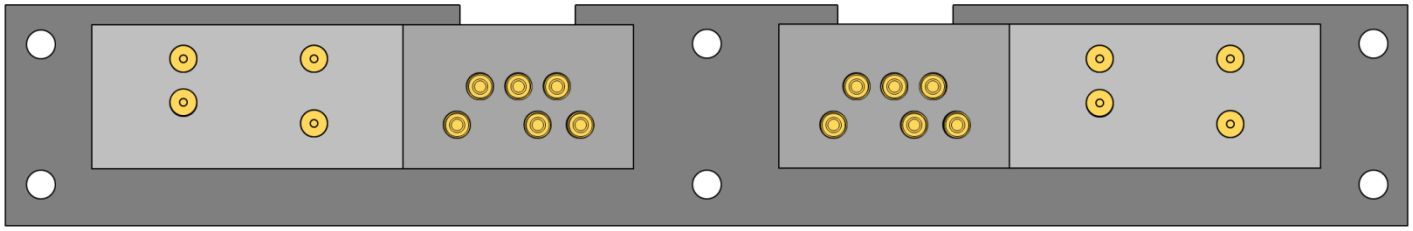

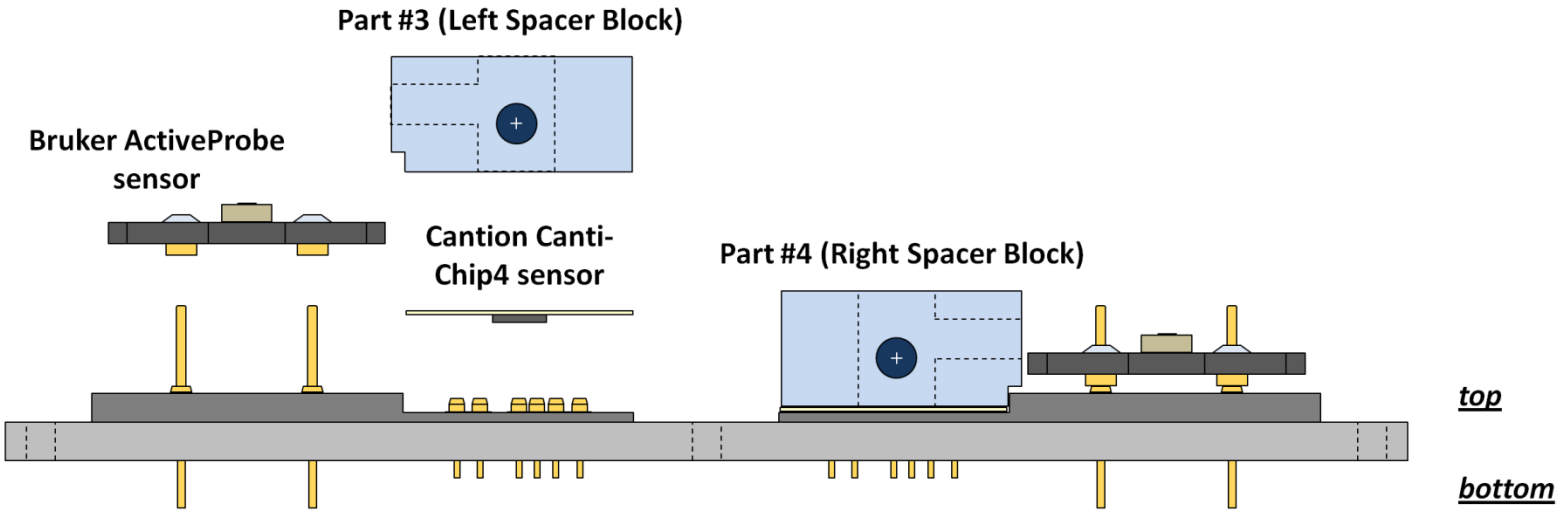

Schematic *Front* View

Drawing Scale: 200%

Twin-Chambered Gas Flow Cell for Sensor Thermal Testing

Albert Loui (loui2@llnl.gov)
(925) 422-2840
8/8/11

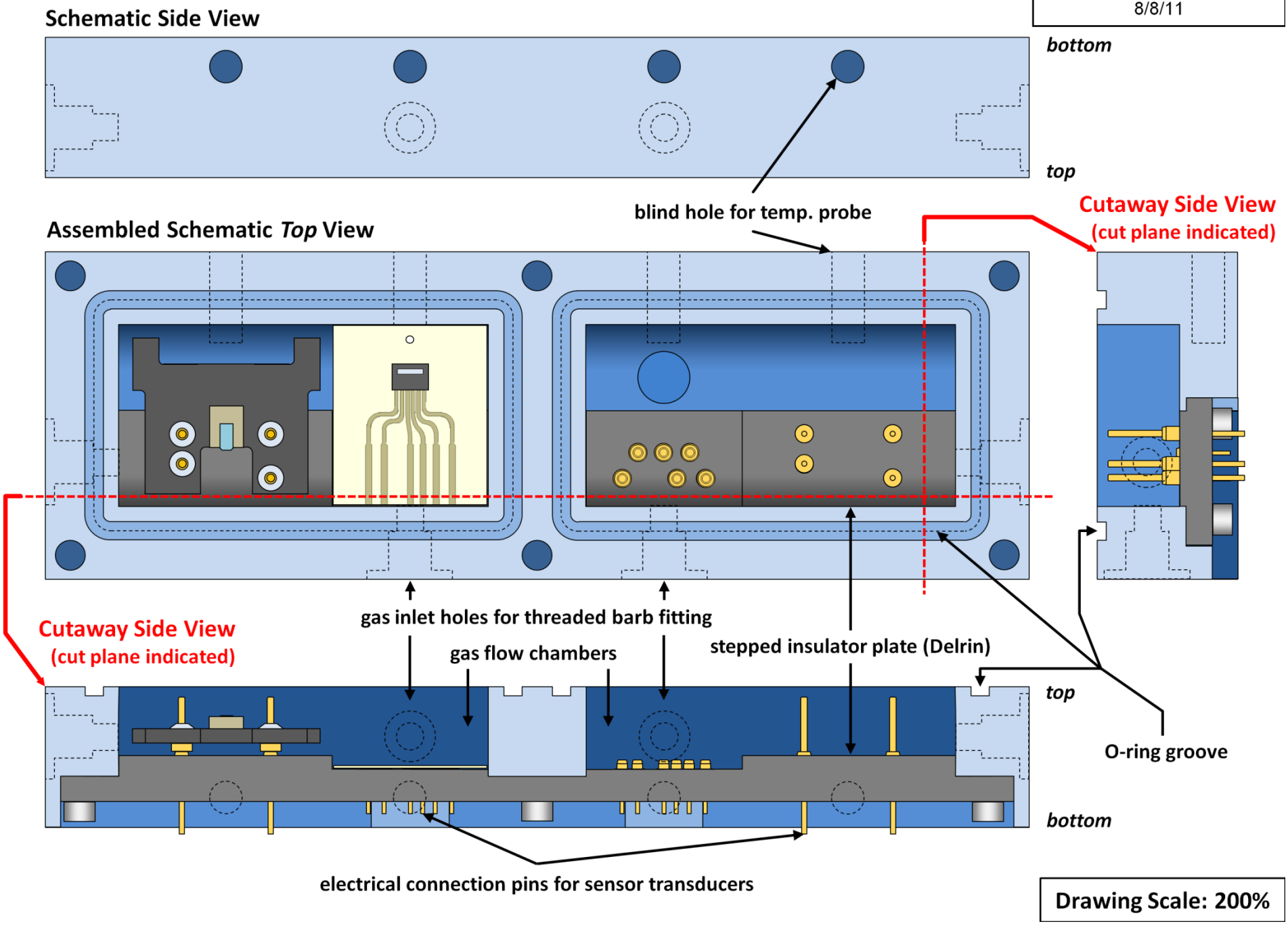

Drawing Scale: 200%

Twin-Chambered Gas Flow Cell for Sensor Thermal Testing

Albert Loui (loui2@llnl.gov)
(925) 422-2840
8/8/11

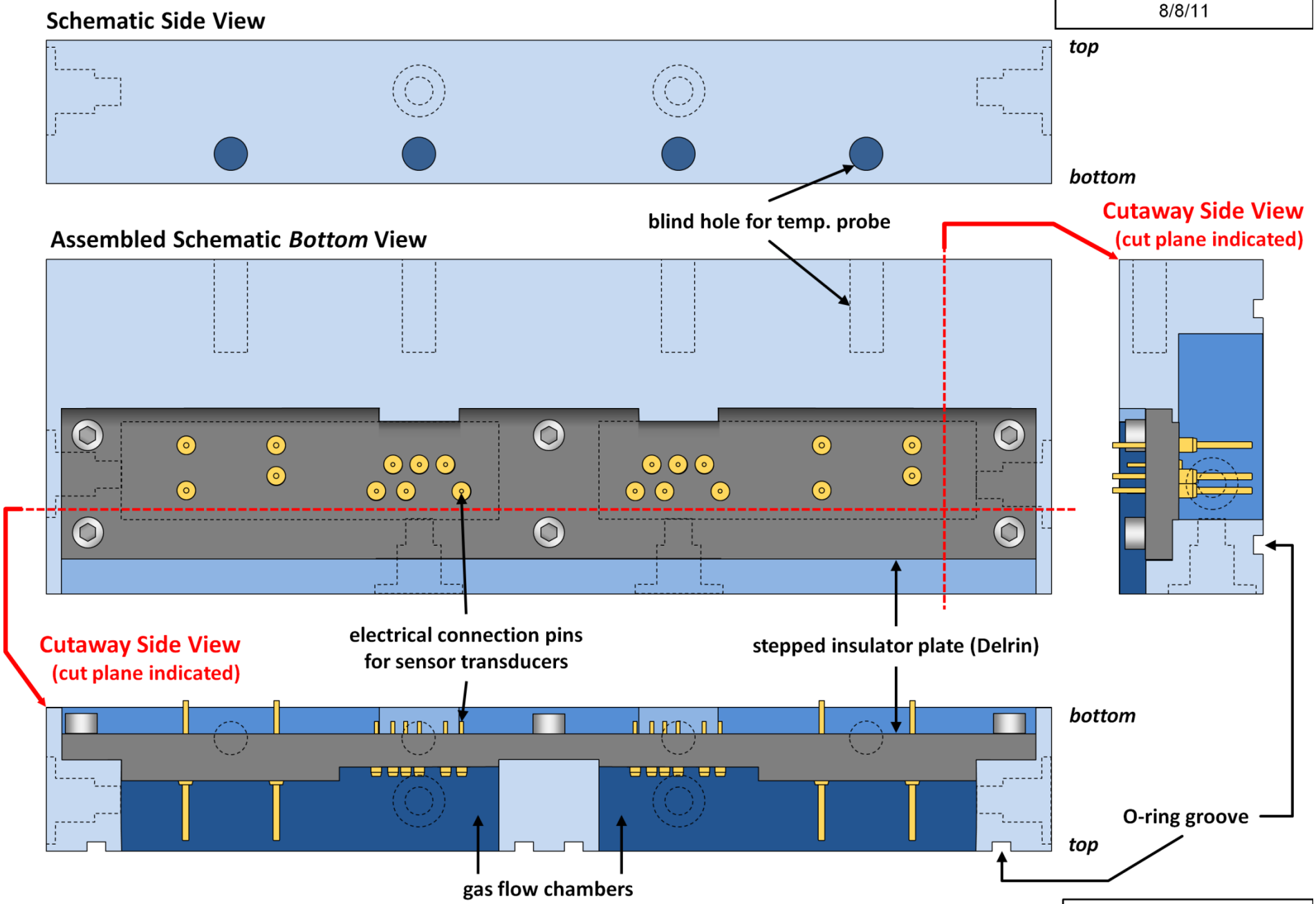

Drawing Scale: 200%

1) Gas Flow Cell (Material: Aluminum; Quantity: 1)

Albert Loui (loui2@llnl.gov)
(925) 422-2840
8/8/11

Schematic *Perspective* View (Top)

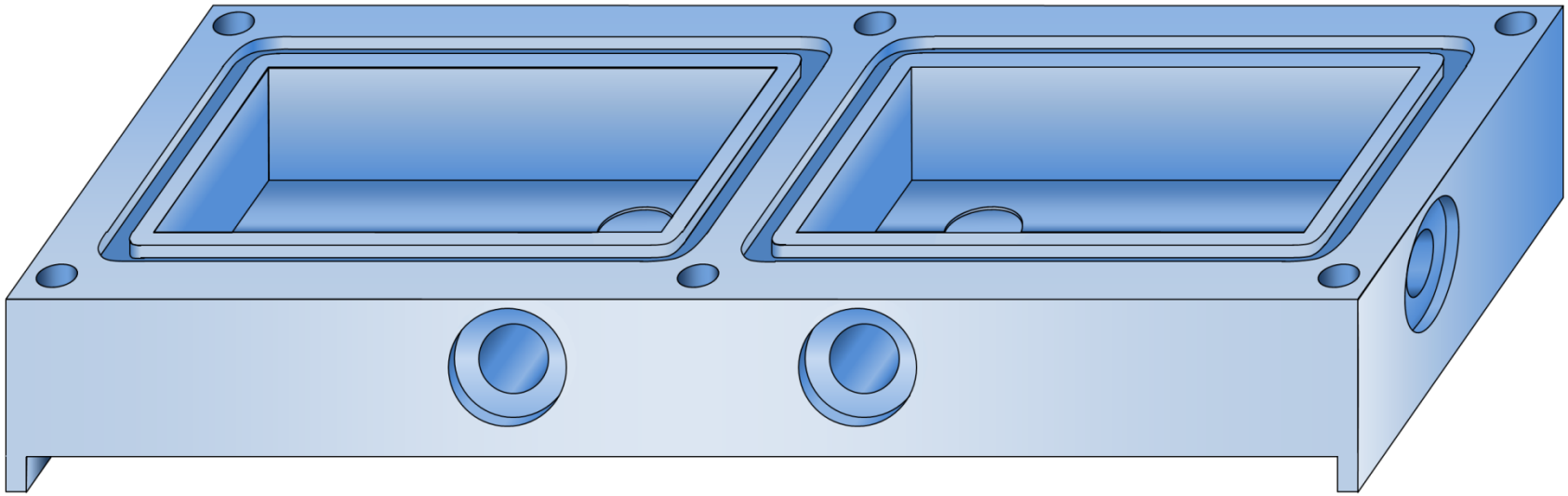

Schematic *Perspective* View (Bottom)

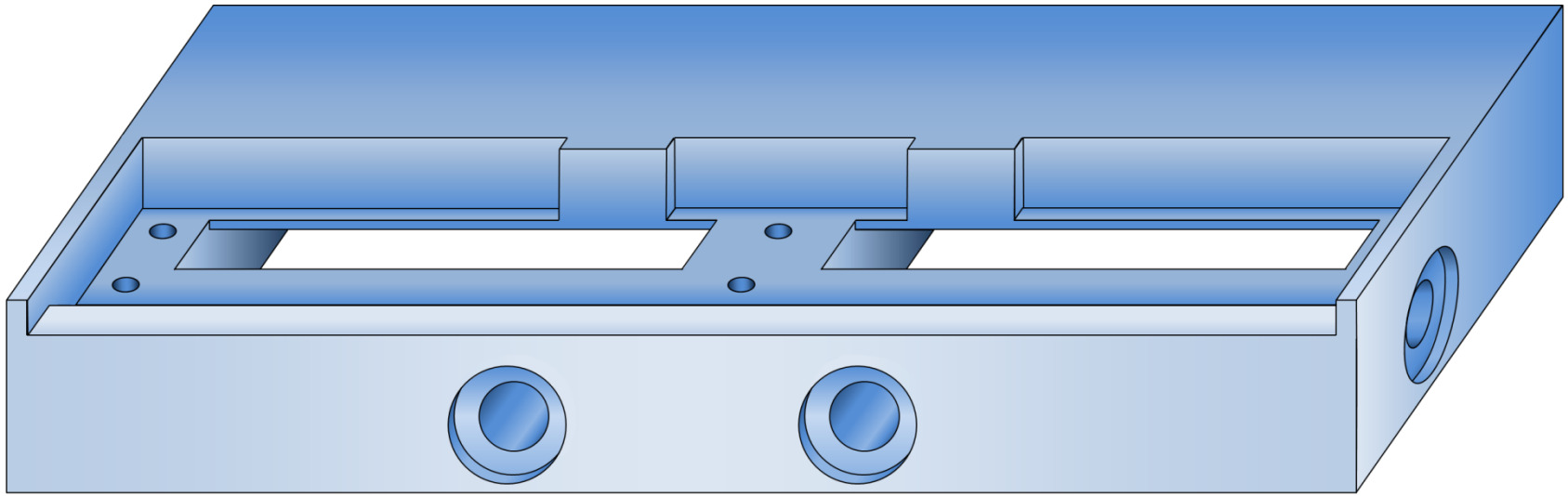

Drawing Scale: 200%

1) Gas Flow Cell (Material: Aluminum; Quantity: 1)

Albert Loui (loui2@llnl.gov)
(925) 422-2840
8/8/11

symmetry axis

Schematic *Rear* View

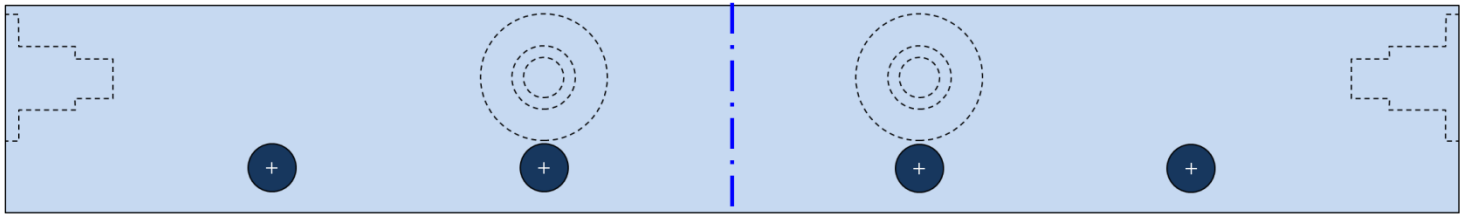

top

bottom

Schematic *Bottom* View

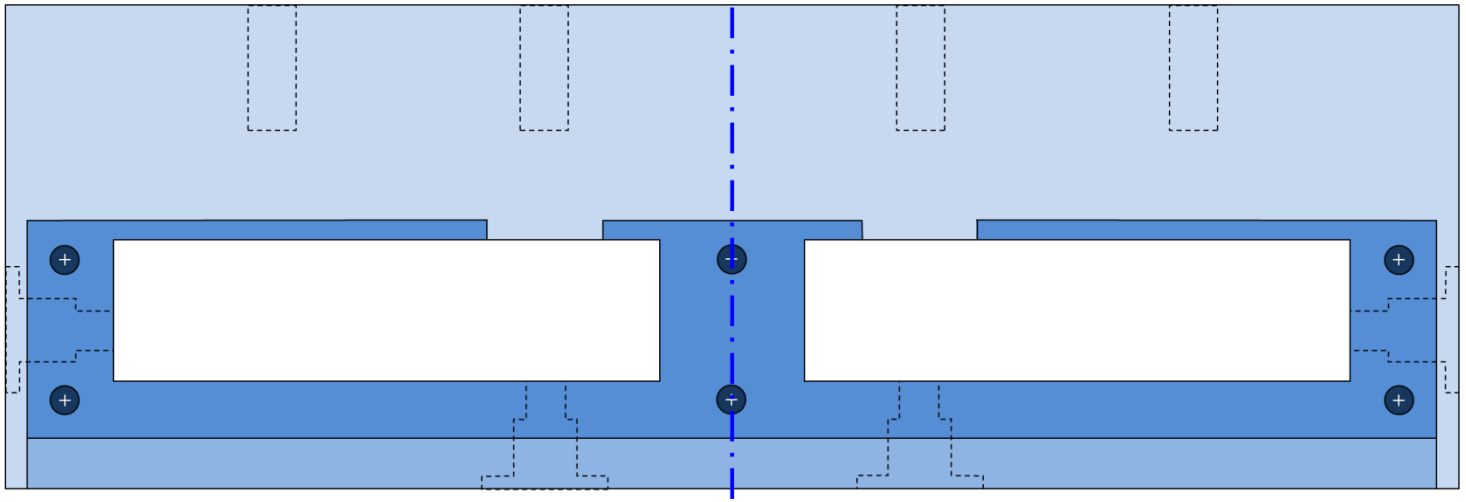

Schematic *Front* View

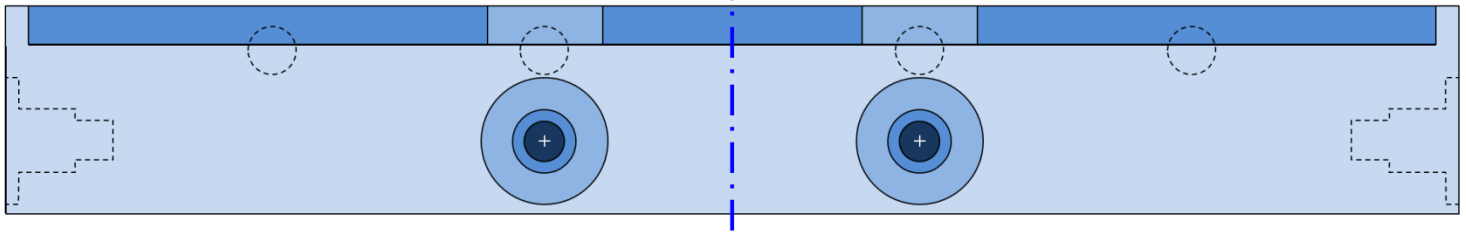

bottom

top

Drawing Scale: 200%

1) Gas Flow Cell (Material: Aluminum; Quantity: 1)

Albert Loui (loui2@llnl.gov)
(925) 422-2840
8/8/11

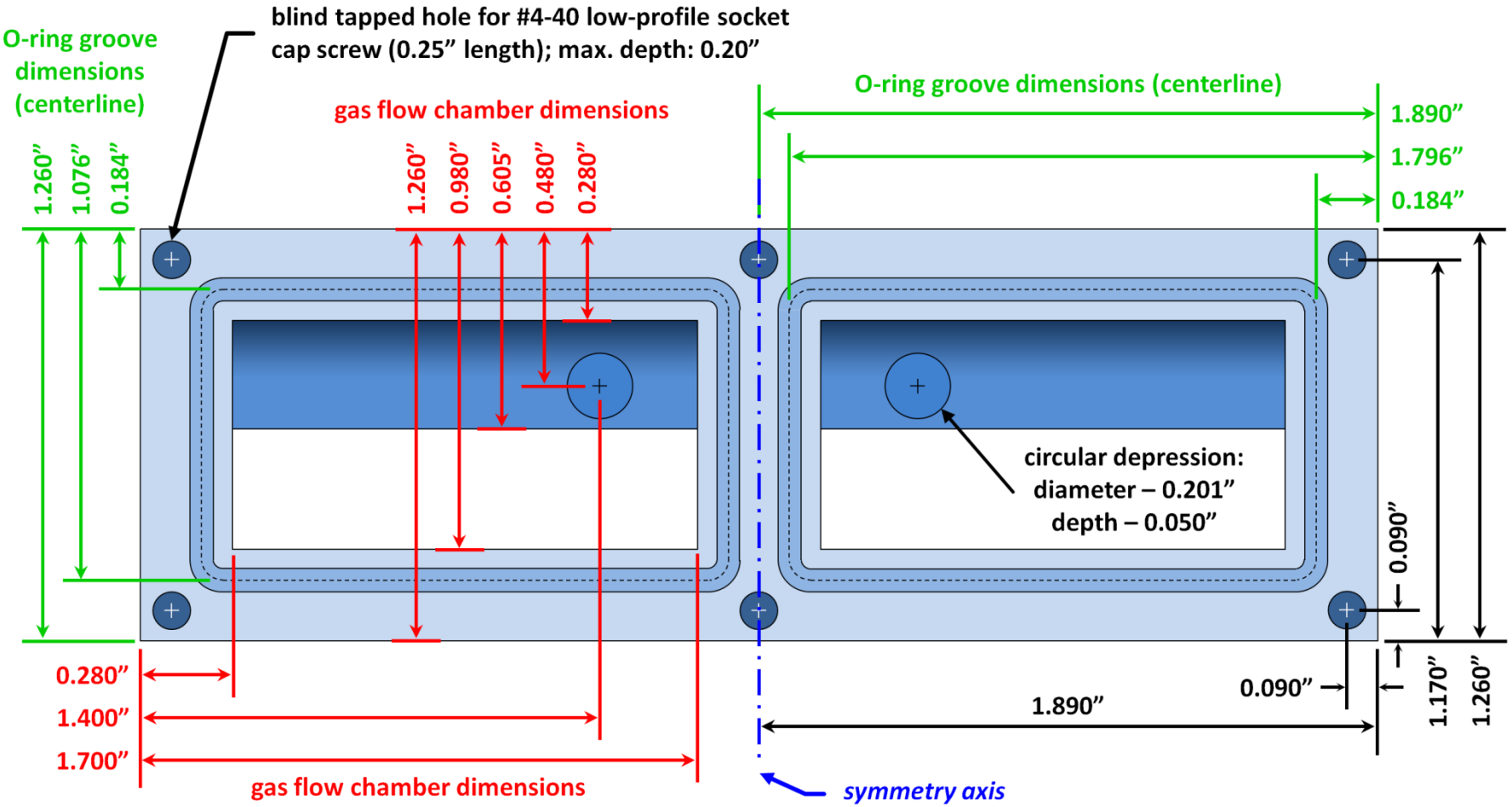

Schematic *Top* View

- O-ring groove dimensions circumscribe the *centerline* of a Viton O-ring (AS568A-029: OD – 1.629", ID – 1.489") with a corner curvature of radius = 0.065"
- Chamfer all sharp edges

Drawing Scale: 200%

1) Gas Flow Cell (Material: Aluminum; Quantity: 1)

Albert Loui (loui2@llnl.gov)
(925) 422-2840
8/8/11

Drawing Scale: 200%

Schematic *Bottom* View

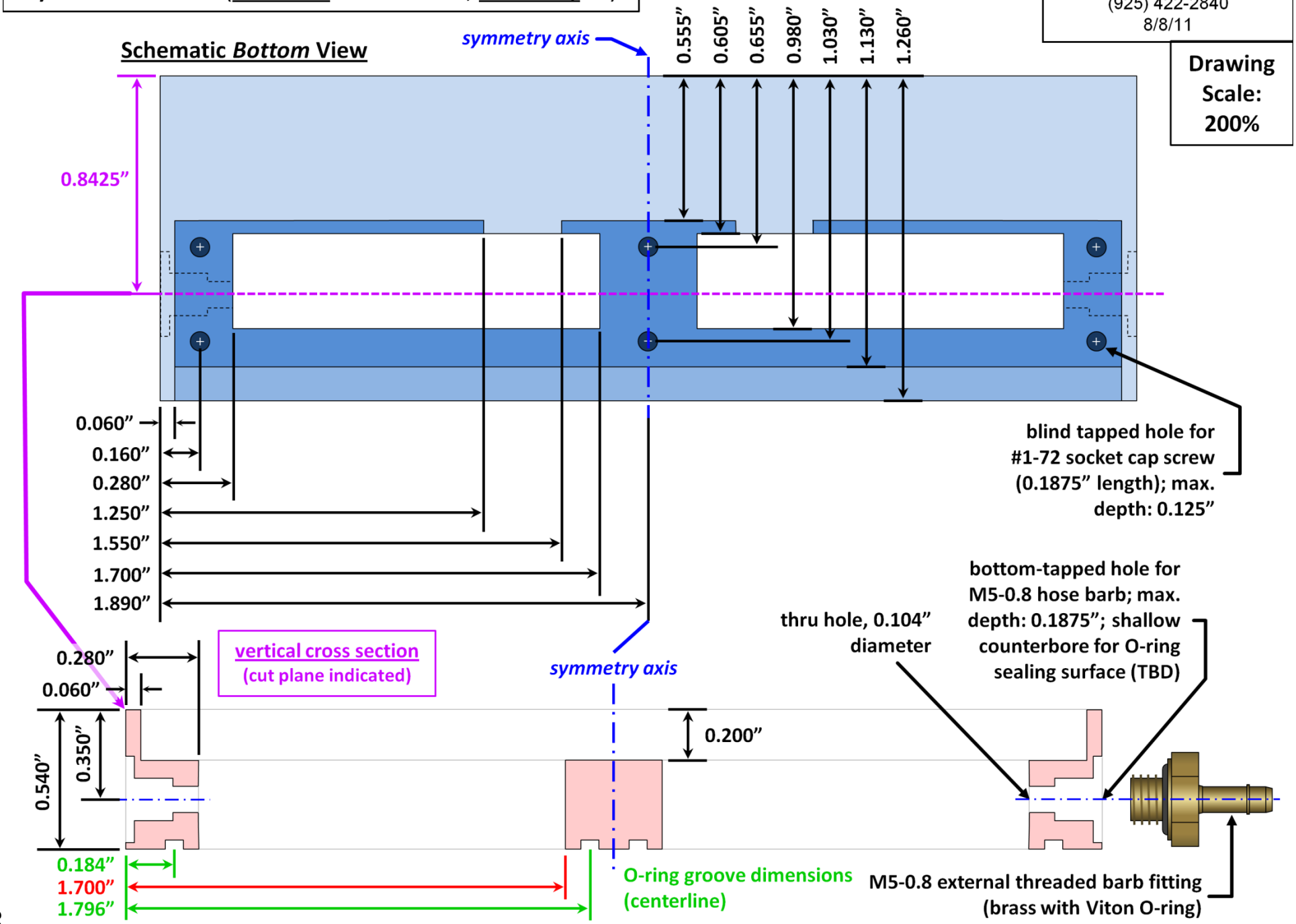

1) Gas Flow Cell (Material: Aluminum; Quantity: 1)

Albert Loui (loui2@llnl.gov)
(925) 422-2840
8/8/11

Drawing Scale: 200%

Schematic *Bottom* View

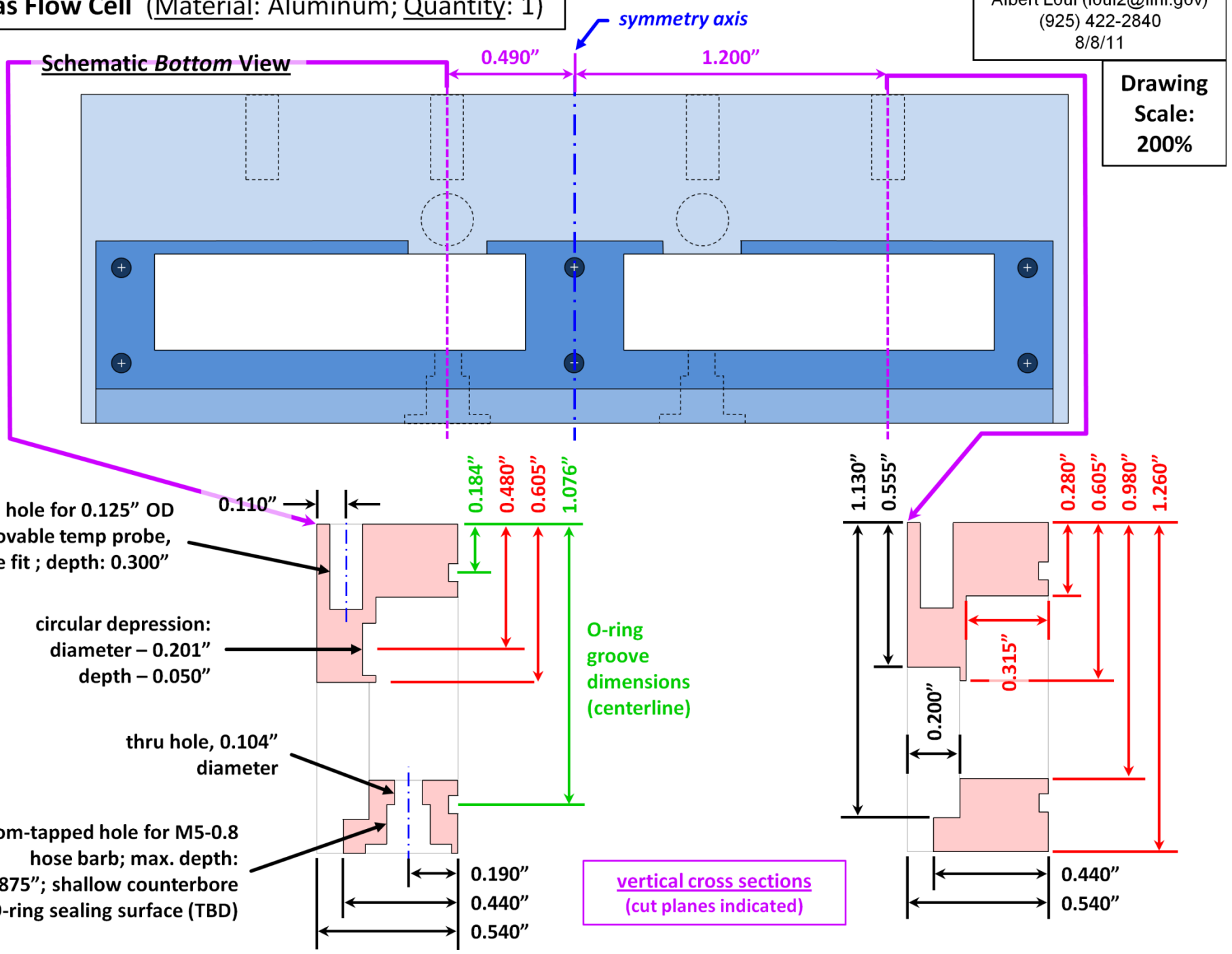

1) Gas Flow Cell (Material: Aluminum; Quantity: 1)

Albert Loui (loui2@llnl.gov)
(925) 422-2840
8/8/11

Drawing Scale: 200%

symmetry axis

Schematic *Bottom* View

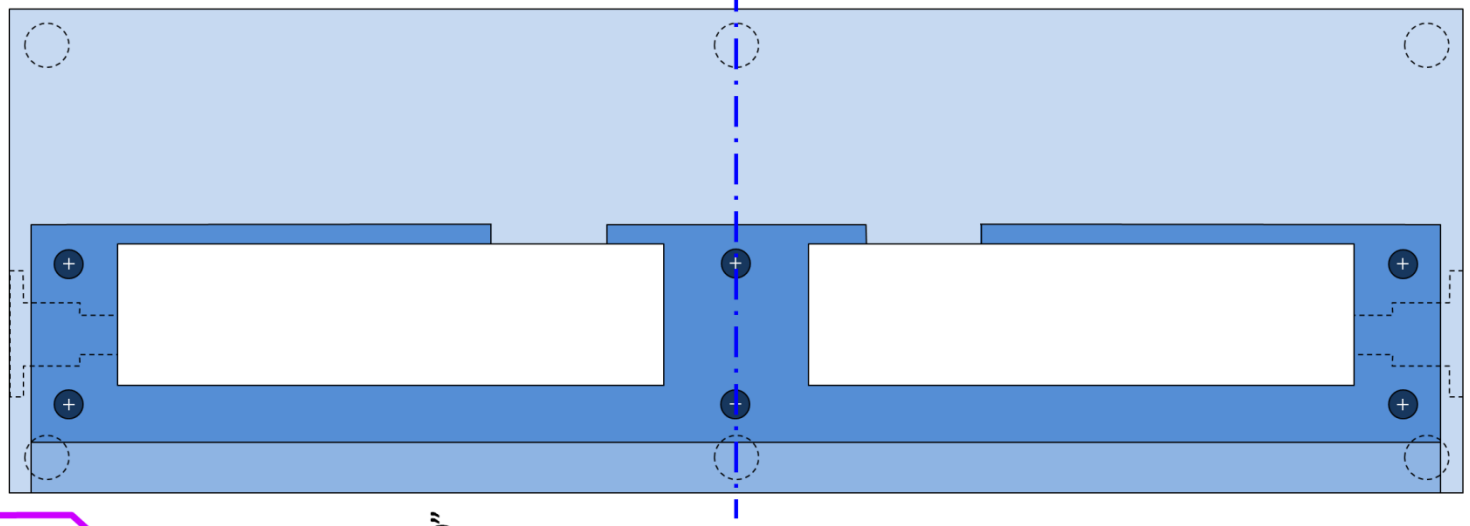

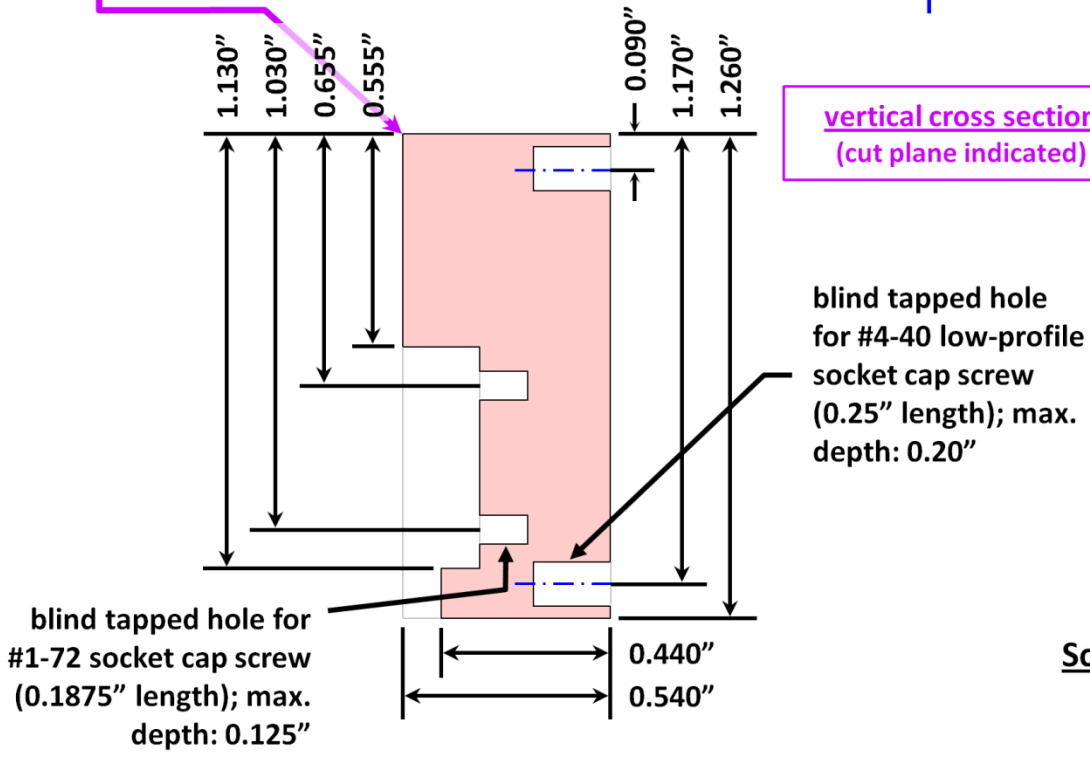

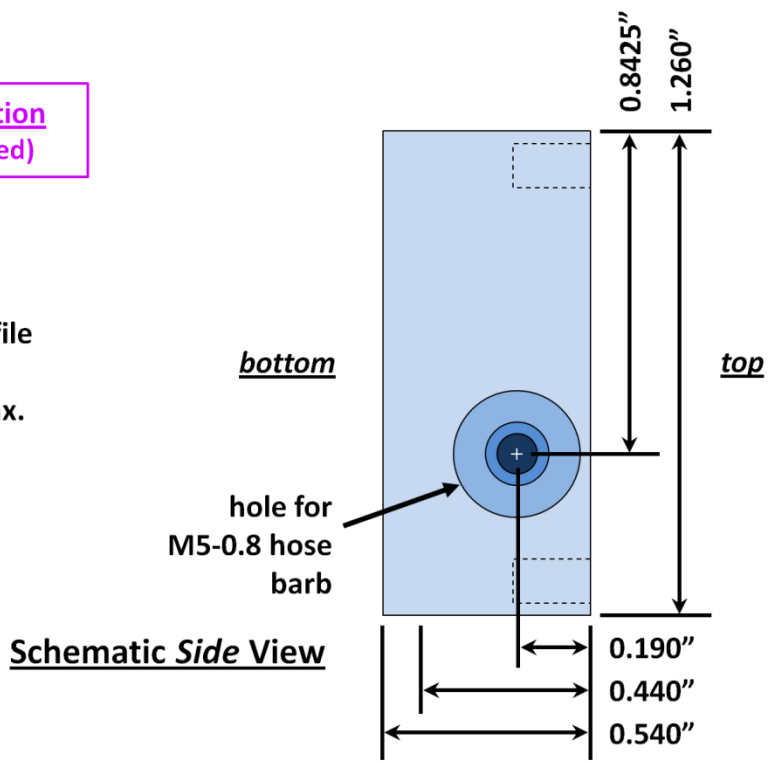

Schematic *Side* View

2) Flow Cell Lid (Material: Aluminum; Quantity: 1)

Albert Loui (loui2@llnl.gov)
(925) 422-2840
8/8/11

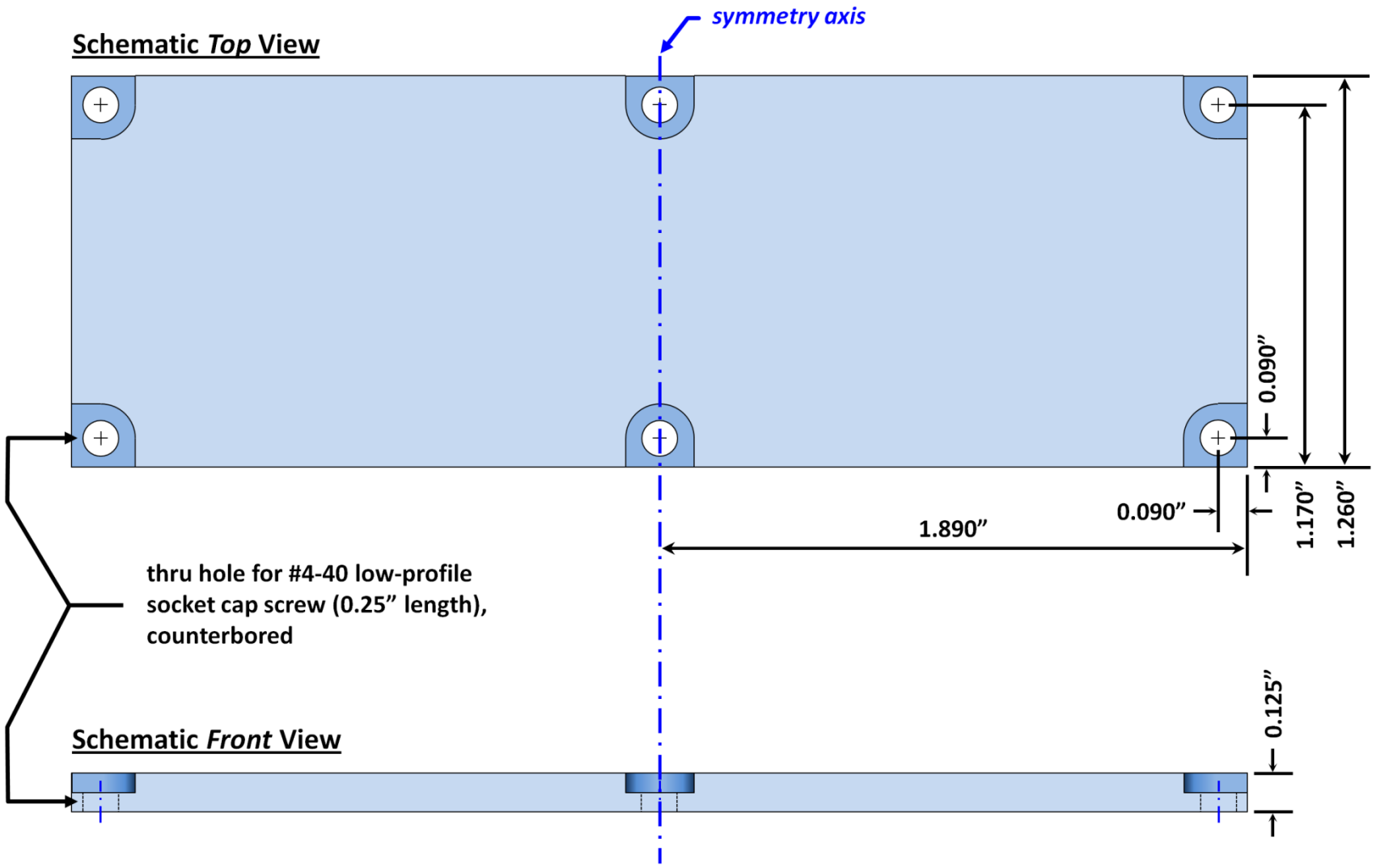

Drawing Scale: 200%

3) Left Spacer Block (Material: Aluminum; Quantity: 1)

Albert Loui (loui2@llnl.gov)
(925) 422-2840
8/8/11

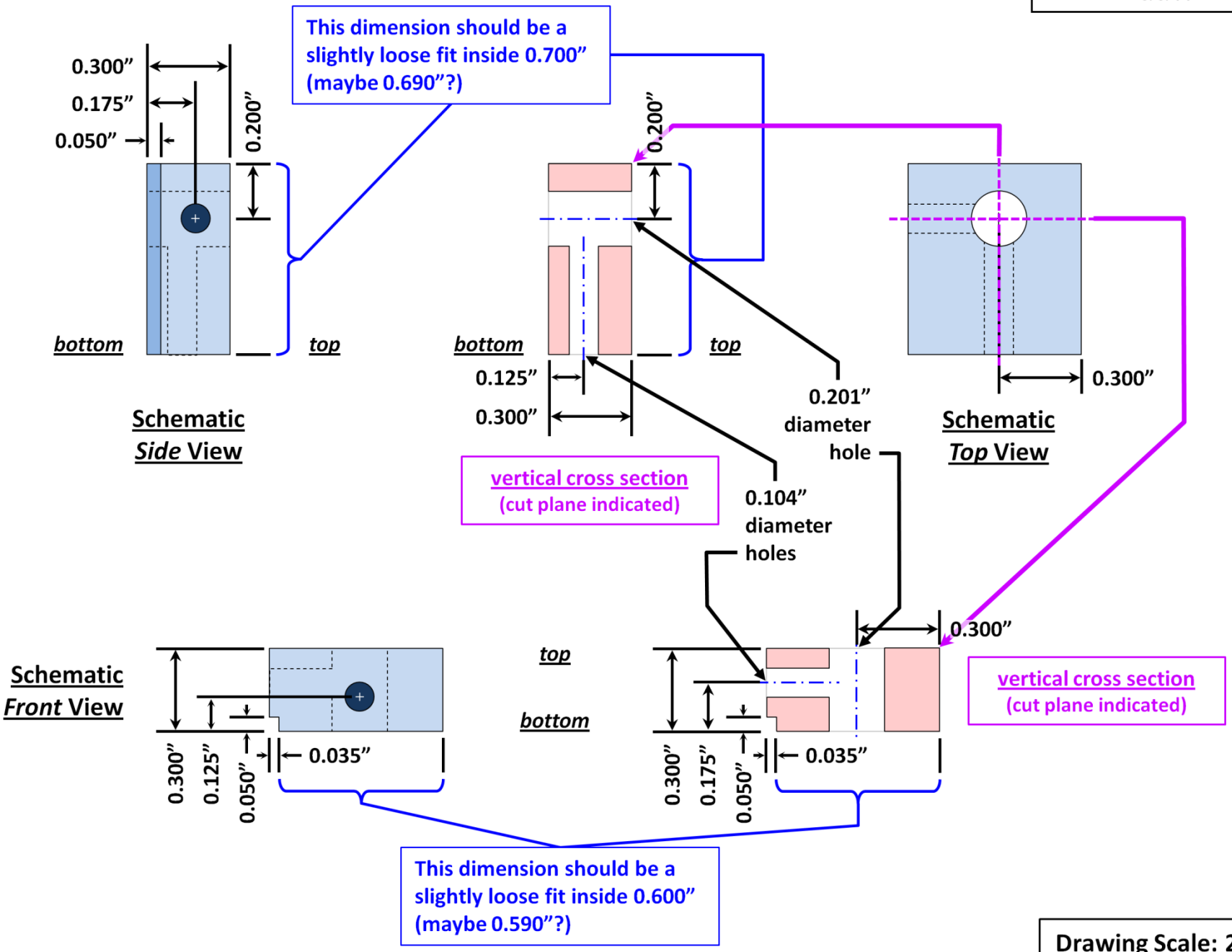

Drawing Scale: 200%

4) Right Spacer Block (Material: Aluminum; Quantity: 1)

Albert Loui (loui2@llnl.gov)
(925) 422-2840
8/8/11

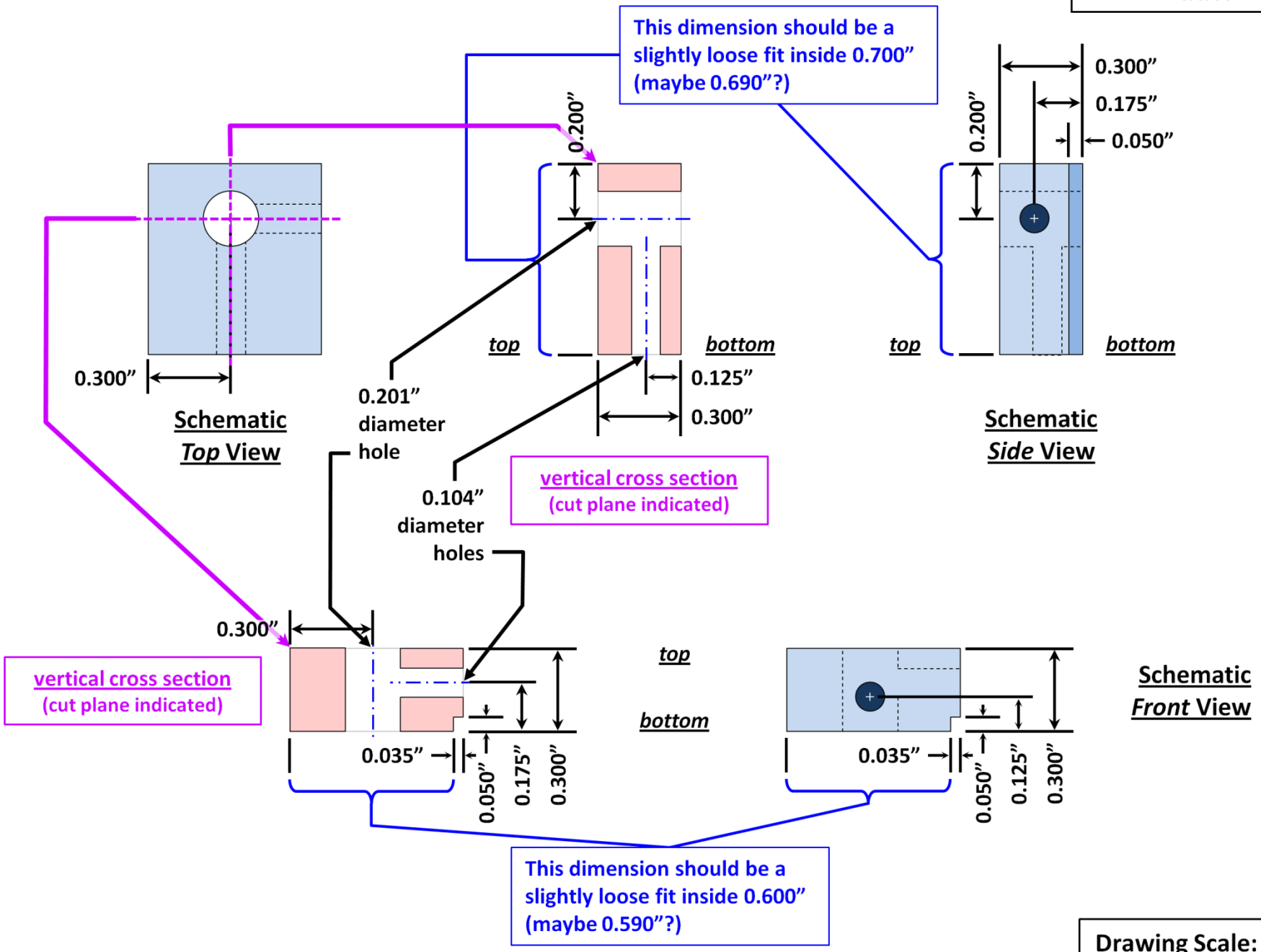

Drawing Scale: 200%

5) Stepped Insulator Plate (Material: Delrin; Quantity: 1)

Albert Loui (loui2@llnl.gov)
(925) 422-2840
8/8/11

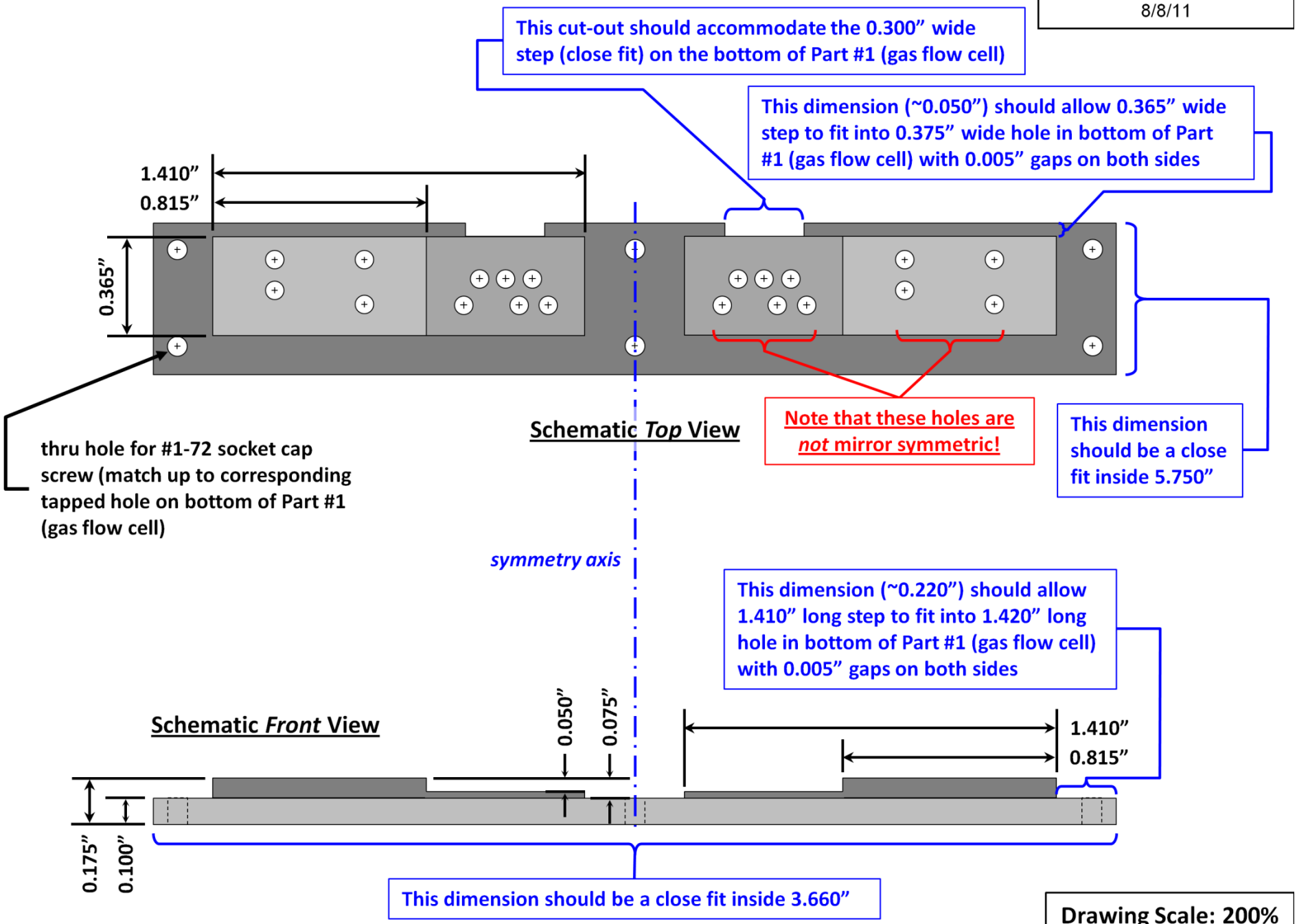

Drawing Scale: 200%

5) Stepped Insulator Plate (Material: Delrin; Quantity: 1)

Albert Loui (loui2@llnl.gov)
(925) 422-2840
8/8/11

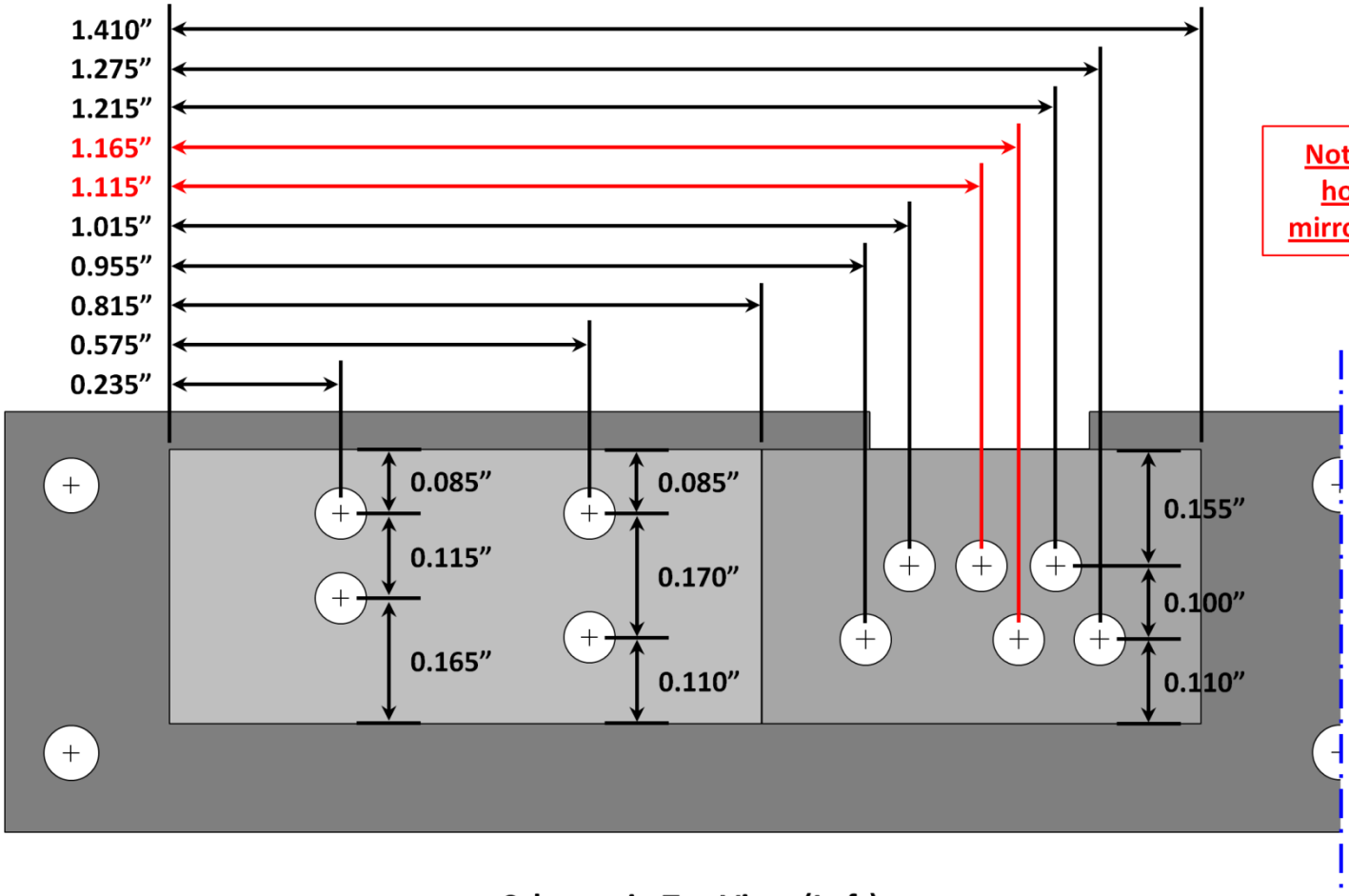

Note that these holes are *not* mirror symmetric!

Schematic *Top* View (Left)

symmetry axis

Drawing Scale: 400%

5) Stepped Insulator Plate (Material: Delrin; Quantity: 1)

Albert Loui (loui2@llnl.gov)
(925) 422-2840
8/8/11

Note that these holes are *not* mirror symmetric!

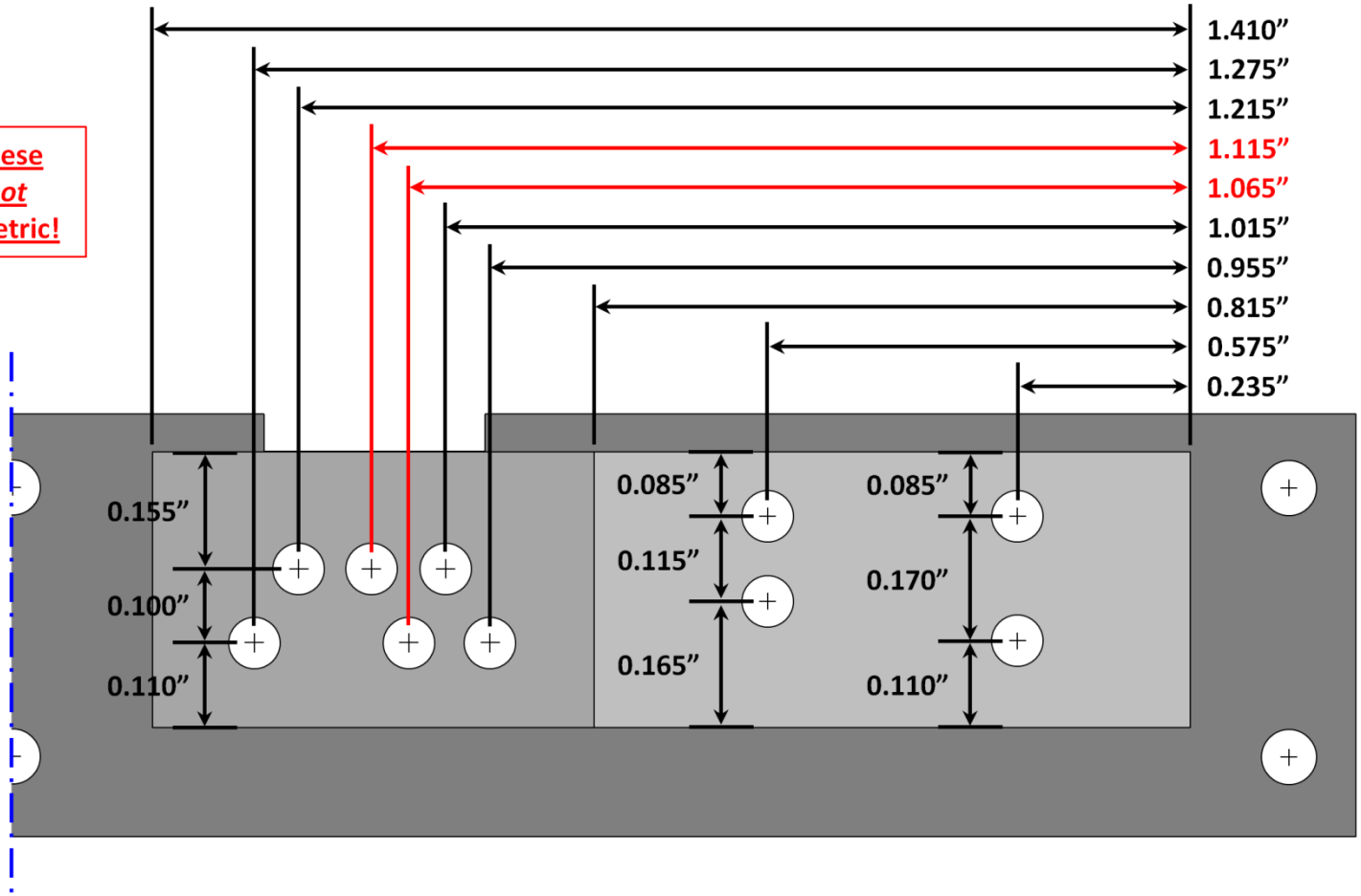

symmetry axis

Schematic *Top* View (Right)

Drawing Scale: 400%

5) Stepped Insulator Plate (Material: Delrin; Quantity: 1)

Albert Loui (loui2@llnl.gov)
(925) 422-2840
8/8/11

Schematic *Front* View

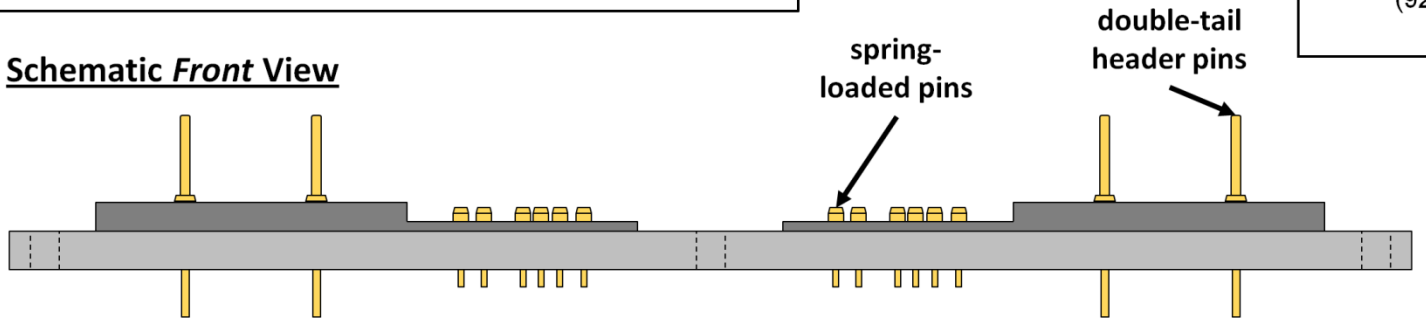

Drawing Scale: 200%

---

spring-loaded pin (Mill-Max 0906-0-15-20-76-14-11-0), brass alloy with 20 μin gold over nickel plating

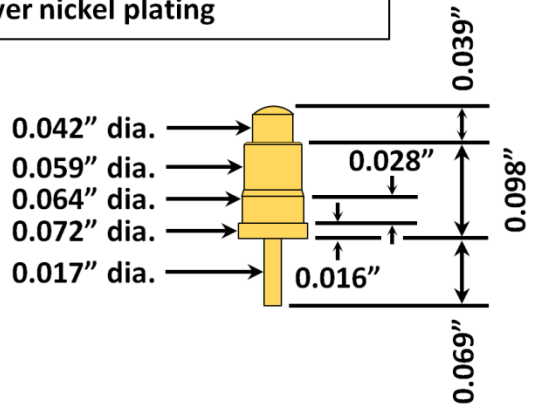

double tail header pin (Mill-Max 3409-1-00-21-00-00-03-0), brass alloy with 20 μin gold over nickel plating

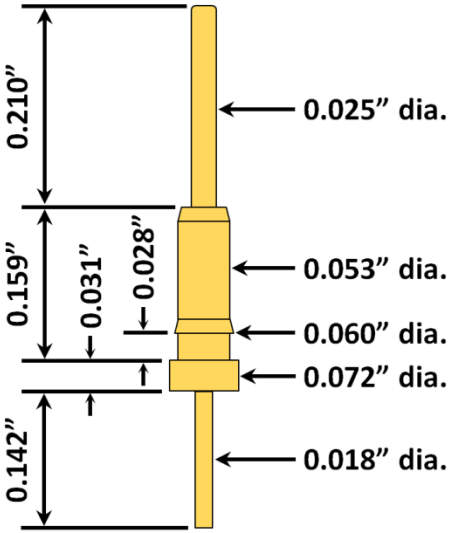

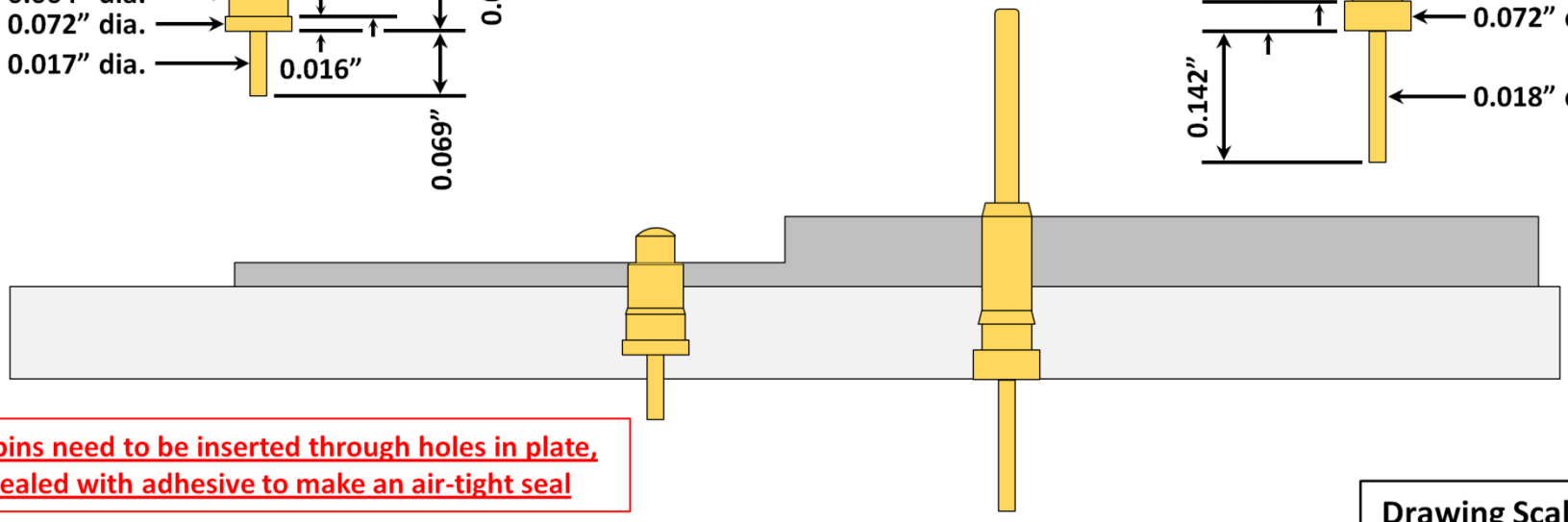

These pins need to be inserted through holes in plate, but sealed with adhesive to make an air-tight seal

Drawing Scale: 500%